Multiple emplacement and exhumation history of the Late Mesozoic Dayunshan-Mufushan batholith in Southeast China and its tectonic significance: 2. Magnetic fabrics and gravity survey

Wenbin Ji, Yan Chen, Ke Chen, Wei Wei, Michel Faure, Wei Lin

AGU PUBLICATIONS

JGR

Journal of Geophysical Research: Solid Earth

RESEARCH ARTICLE
10.1002/2017JB014598

This article is a companion to Ji et al. (2017) https://doi.org/10.1002/2017JB014597.

Key Points:
- The Dayunshan-Mufushan batholith recorded a multiple emplacement and exhumation history
- An integrated multidisciplinary investigation improves our understanding on the Late Mesozoic tectonomagmatism in southeast China
- A two-stage construction of the batholith with distinct tectonic regimes from compression to extension has been established

Supporting Information:
- Supporting Information S1

Correspondence to:
W. Lin,
linwei@mail.iggcas.ac.cn

Citation:
Ji, W., Chen, Y., Chen, K., Wei, W., Faure, M., & Lin, W. (2018). Multiple emplacement and exhumation history of the Late Mesozoic Dayunshan-Mufushan batholith in southeast China and its tectonic significance: 2. Magnetic fabrics and gravity survey. *Journal of Geophysical Research: Solid Earth*, *123*. https://doi.org/10.1002/2017JB014598

Received 25 JUN 2017
Accepted 17 NOV 2017
Accepted article online 7 DEC 2017

Multiple Emplacement and Exhumation History of the Late Mesozoic Dayunshan-Mufushan Batholith in Southeast China and Its Tectonic Significance: 2. Magnetic Fabrics and Gravity Survey

Wenbin Ji[1,2], Yan Chen[2], Ke Chen[3], Wei Wei[1,2], Michel Faure[2], and Wei Lin[1]

[1]State Key Laboratory of Lithospheric Evolution, Institute of Geology and Geophysics, Chinese Academy of Sciences, Beijing, China, [2]Institut des Sciences de la Terre d'Orléans, UMR 7327, Université d'Orléans, Orléans, France, [3]Oil and Gas Survey, China Geological Survey, Beijing, China

Abstract The Late Mesozoic magmatic province is a prominent feature of the South China Block (SCB). However, the tectonic regimes associated with the magmatism are still elusive. A combined anisotropy of magnetic susceptibility and gravity study has been carried out to determine the fabric patterns and shape at depth of the Dayunshan-Mufushan composite batholith in the north-central SCB. This is a companion paper to Part 1 that presented the structural and geochronological data of this batholith. The magnetic fabrics in the batholith interior predominantly reflect magma flow structures. Two distinct patterns of the magnetic lineations are defined, around NNE-SSW and WNW-ESE trends for the early-stage and late-stage intrusions of the batholith, respectively. The gravity survey reveals that the early-stage intrusion has a main feeder zone located below its northern part, while several linear feeder zones trending NNE-SSW are inferred for the late-stage intrusion. Integrating all results, a two-stage construction of the batholith with distinct tectonic regimes has been established. It is concluded that the early-stage intrusion experienced a southward magma transport during its emplacement, partially assisted by far-field compression from the north at ca. 150 Ma. Conversely, the emplacement and exhumation of the late-stage intrusion was accommodated by a NW-SE crustal stretching involving a lateral magma expansion above the multiple feeder zones (likely corresponding to extensional fractures) and ductile shearing during 132–95 Ma localized mainly along the Dayunshan detachment fault. Finally, we discuss the geodynamic linkage between the paleo-Pacific subduction and the Late Mesozoic tectonomagmatism in the SCB.

1. Introduction

The eastern Asian realm experienced a tectonic switch during the Mesozoic, since it evolved from the closure of the Paleo-Tethyan Ocean into the subduction of the Pacific Ocean. In eastern China, the Late Mesozoic geological evolution characterized by large-scale intracontinental deformation and magmatism is traditionally referred to as the Yanshanian (i.e., Jurassic-Cretaceous period) cycle (e.g., Davis et al., 2001; Dong et al., 2015; Faure, Lin, & Chen, 2012; Li et al., 2012; J. H. Li et al., 2014; Lin, Faure, et al., 2013). There, compressional and extensional events have been distinguished by different authors, leading to confusion in understanding the complex tectonic scenarios. It is well acknowledged that Cretaceous metamorphic core complexes (MCCs) are widely developed in the North China Craton (NCC) and its adjacent regions, indicative of a widespread NW-SE extension coeval with lithospheric thinning (e.g., Charles et al., 2012, 2011; Ji, Lin, Faure, Shi, et al., 2017; Lin, Faure, et al., 2013; Lin et al., 2015; Lin & Wang, 2006; Liu et al., 2013; T. Wang et al., 2011, 2012). In fact, the South China Block (SCB) also experienced continental extension during the Late Mesozoic. Jurassic-Cretaceous plutonic rocks occupy a vast area in southeast China (i.e., the eastern SCB) and often form uplifted belts in contact with nearby basins along brittle or locally ductile normal faults. Such a configuration has been described as the "southeast China basin and range tectonics" by many authors (Gilder et al., 1996, 1991; Li, 2000; J. H. Li et al., 2014; Shu et al., 2009; Wang & Shu, 2012). However, only several domal structures have been documented in the hinterland of the SCB, such as the Wugongshan, Lushan, Hongzhen, Hengshan, and Huangling massifs (Figure 1; for further discussion, see "Part 1: Structural analysis and geochronological constraints" of Ji, Faure, et al., 2017). These massifs are mainly thermal domes related to plutonism rather than MCCs, implying that the overall continental extension in southeast China seems to be weak. Owing to the limited exposure of deep crustal ductile structures, the kinematic pattern and precise

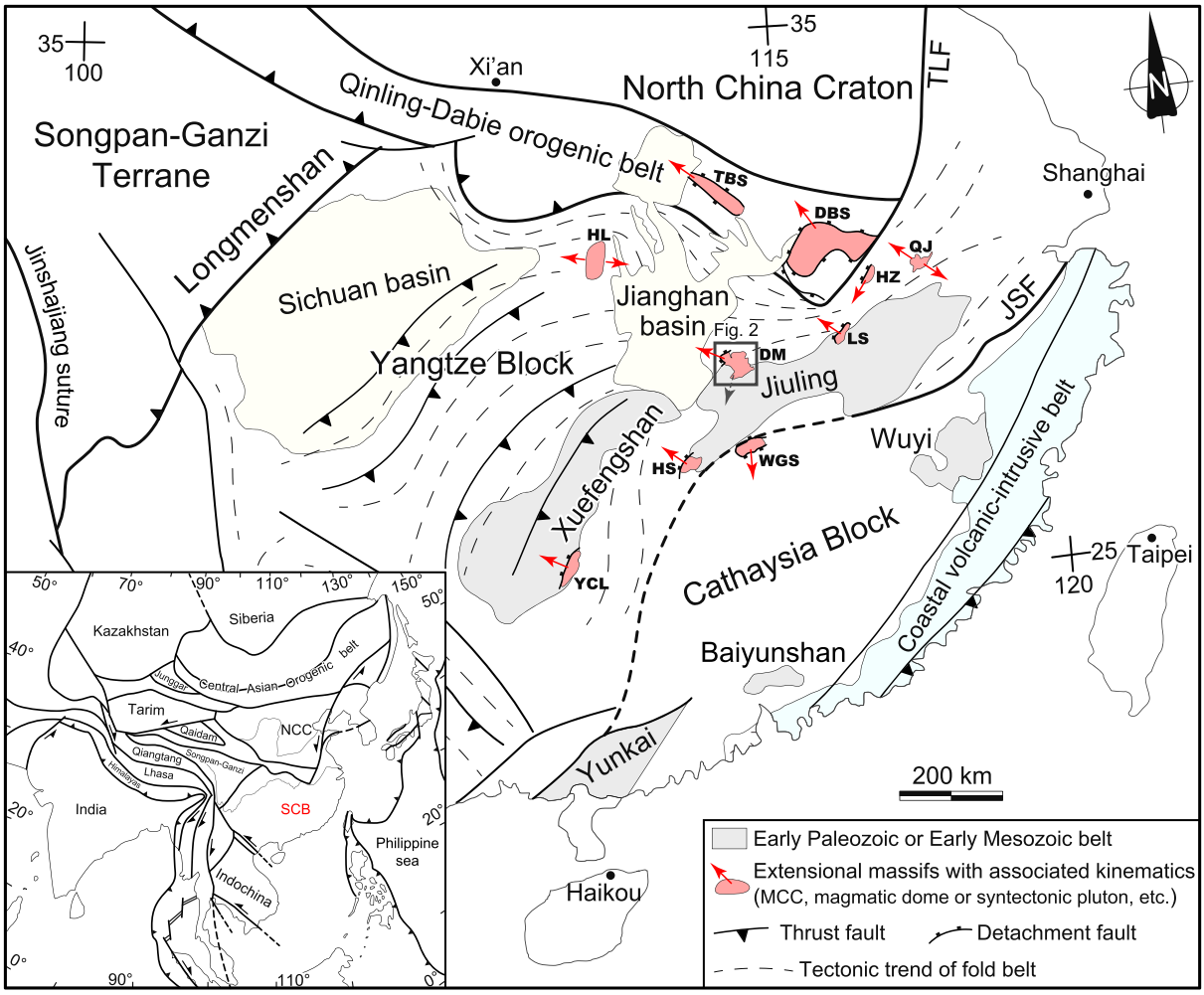

Figure 1. Tectonic sketch of the SCB and location of the Dayunshan-Mufushan batholith. NCC, North China Craton; SCB, South China Block; TLF, Tan-Lu fault; and JSF, Jiangshan-Shaoxing fault, representing the Neoproterozoic suture zone between the Yangtze and Cathaysia blocks. Several Late Mesozoic extensional massifs in South China: Tongbaishan (TBS), Dabieshan (DBS), Huangling (HL), Qingyang-Jiuhua (QJ), Hongzhen (HZ), Lushan (LS), Wugongshan (WGS), Dayunshan-Mufushan (DM), Hengshan (HS), and Yuechengling (YCL). See Part 1 for references.

timing of the Late Mesozoic extensional tectonics in the SCB remain inconclusive. Therefore, structural studies of plutonic rocks are needed in order to detect the crustal deformation.

Previous works on the Late Mesozoic plutons in southeast China, as well as the associated volcanics, have mostly focused on their geochronological framework and geochemical characteristics. Several geodynamic models involving the paleo-Pacific (or Pacific) subduction beneath the SCB have been proposed accordingly to account for the origin and temporal-spatial evolution of such a magmatic province (e.g., Chen, Lee, & Shinjo, 2008; F. Y. Wang et al., 2011; Ji, Lin, Faure, Chen, et al., 2017; Jiang et al., 2015; L. Liu, Xu, & Xia, 2016; Li & Li, 2007; Ling et al., 2009; Liu et al., 2012; Wu et al., 2012; Z. Li, Qiu, & Yang, 2014; Zhou & Li, 2000; Zhou et al., 2006). However, there is still no consensus on the subduction initiation (e.g., Permian, Late Triassic, Early Jurassic, or Early Cretaceous) and style (e.g., change of the slab dip angle or subduction direction, flat-slab subduction and subsequent slab foundering, slab rollback, ridge subduction, and repeated slab advance-retreat) of the subducted plate. The lack of structural constraints makes difficult the assessment of the tectonic regimes (compression, extension, or strike slip) that are associated with the magmatism in the overriding continental plate. Pluton emplacement processes contain significant information on the concomitant regional stress fields, since magma ascent and final emplacement are usually controlled by both internal dynamics and external tectonism (Bouchez, Hutton, & Stephens, 1997; Brown, 2013; Castro, 1987;

Hutton, 1988; Paterson et al., 1998). In particular, determining the fabric patterns and shape at depth of plutons is crucial to address their emplacement modes, but only a few such work have been carried out in south China (Feng et al., 2012; Wei, Chen, et al., 2014; Wei et al., 2016; Wei, Martelet, et al., 2014; Zhang et al., 2008). The Dayunshan-Mufushan batholith that intruded into the Xuefengshan-Jiuling belt in the central SCB comprises Late Jurassic to Early Cretaceous granitic intrusions. In order to reveal its emplacement-exhumation history and tectonic significance, an integrated multidisciplinary investigation including structural geology, geochronology, anisotropy of magnetic susceptibility (AMS), and gravity methods has been conducted. Our study not only brings new insights on the Late Mesozoic tectonomagmatism in southeast China but also provides a typical example dealing with the construction of composite batholiths. This work consists of two parts: Part 2 presented hereunder concerns magnetic fabrics and gravity survey; it is a companion paper to Part 1 focusing on structural analysis and geochronological constraints.

2. Geological Setting

2.1. Regional Framework

The SCB is bounded to the north by the NCC and to the west and southwest by the Tibetan Plateau and Indochina block, respectively (Figure 1). An overview of the major tectonic events in the SCB has been given in Part 1. The SCB experienced a complex tectonic history after its early Neoproterozoic (before ca. 820 Ma) amalgamation between the Yangtze and Cathaysia blocks along the Jiangnan orogen (for a review, see Wang et al., 2013). Two episodes of intracontinental orogeny with regional metamorphism and magmatism, respectively, during the Early Paleozoic and the Early Mesozoic significantly reworked the Precambrian tectonic framework of the SCB to different extent (e.g., Charvet et al., 2010; Chu, Faure, Lin, & Wang, 2012; Chu, Faure, Lin, Wang, & Ji, 2012; Chu & Lin, 2014; Faure et al., 2009; Lin, Wang, & Chen, 2008; Shu et al., 2014, 2015; Z. X. Li et al., 2010). The architecture of the NE-SW trending Xufengshan-Jiuling belt in the central SCB that superposed upon the preexisting Jiangnan orogen was chiefly built by the Triassic tectonism, accommodating a SE directed intracontinental subduction coeval with continental collision between the SCB and Indochina block to the south (Faure et al., 2016). As mentioned before, the Late Mesozoic geology of the eastern SCB is featured by widespread magmatism and numerous small rift basins, indicating an overall extensional tectonic regime related to the paleo-Pacific subduction (e.g., J. H. Li et al., 2014; Shu et al., 2009; Wang & Shu, 2012; Zhou & Li, 2000; Zhou et al., 2006). However, the western SCB seems to be dominated by a compressional tectonic regime, for instance, the Yangtze foreland belt of the Qinling-Dabie orogen and the thin-skinned tectonic system between the Sichuan basin and Xuefengshan belt, respectively, recorded SW directed and NW directed folding and thrusting during the Late Mesozoic (e.g., Li et al., 2012; Liu et al., 2015; Yan et al., 2003).

In the middle segment of the Xufengshan-Jiuling belt, several Late Mesozoic peraluminous granitic plutons including the Dayunshan-Mufushan batholith represent the western front of the southeast China magmatic province. The country rocks of these granitoids are composed of a suite of slightly metamorphosed Neoproterozoic flysch series (i.e., the Lengjiaxi Group, representing the basement sequences exposed in the Jiangnan domain) and the unconformably overlying pre-Mesozoic shallow-marine carbonate and siliciclastic rocks. These strata were strongly folded by polyorogenic deformation prior to the superposition of NE striking fault basins that were filled with Cretaceous-Paleogene continental red beds (Chu & Lin, 2014). More recently, a detailed investigation on geochronology and petrogenesis of representative plutons in this area has been carried out (Ji, Lin, Faure, Chen, et al., 2017). It is shown that the studied plutons were emplaced at three phases, namely, 151–146 Ma, 132–127 Ma, and ca. 117 Ma. Their source rocks were probably derived from partial melting of the Lengjiaxi Group and its underlying formations.

2.2. The Dayunshan-Mufushan Batholith

The Dayunshan-Mufushan batholith is a large, composite granitic massif (Figure 2). According to previous and our own surveys (Bureau of Geology and Mineral Resources of Hunan Province, 1988; Ji, Lin, Faure, Chen, et al., 2017; Wang et al., 2014), we subdivided this batholith into two major magmatic suites in view of geochronology and petrology. Their respective petrographic and structural features are described below:

1. *An early-stage (Late Jurassic) biotite-rich intrusion* consists of biotite monzogranite and subordinate biotite granodiorite. This pluton was dismembered by the late-stage intrusion, with three main parts distributed in the north and south of the batholith. Porphyritic biotite monzogranite as the predominant rock type is composed of plagioclase, K-feldspar, quartz, and biotite. In some places, secondary muscovite, locally

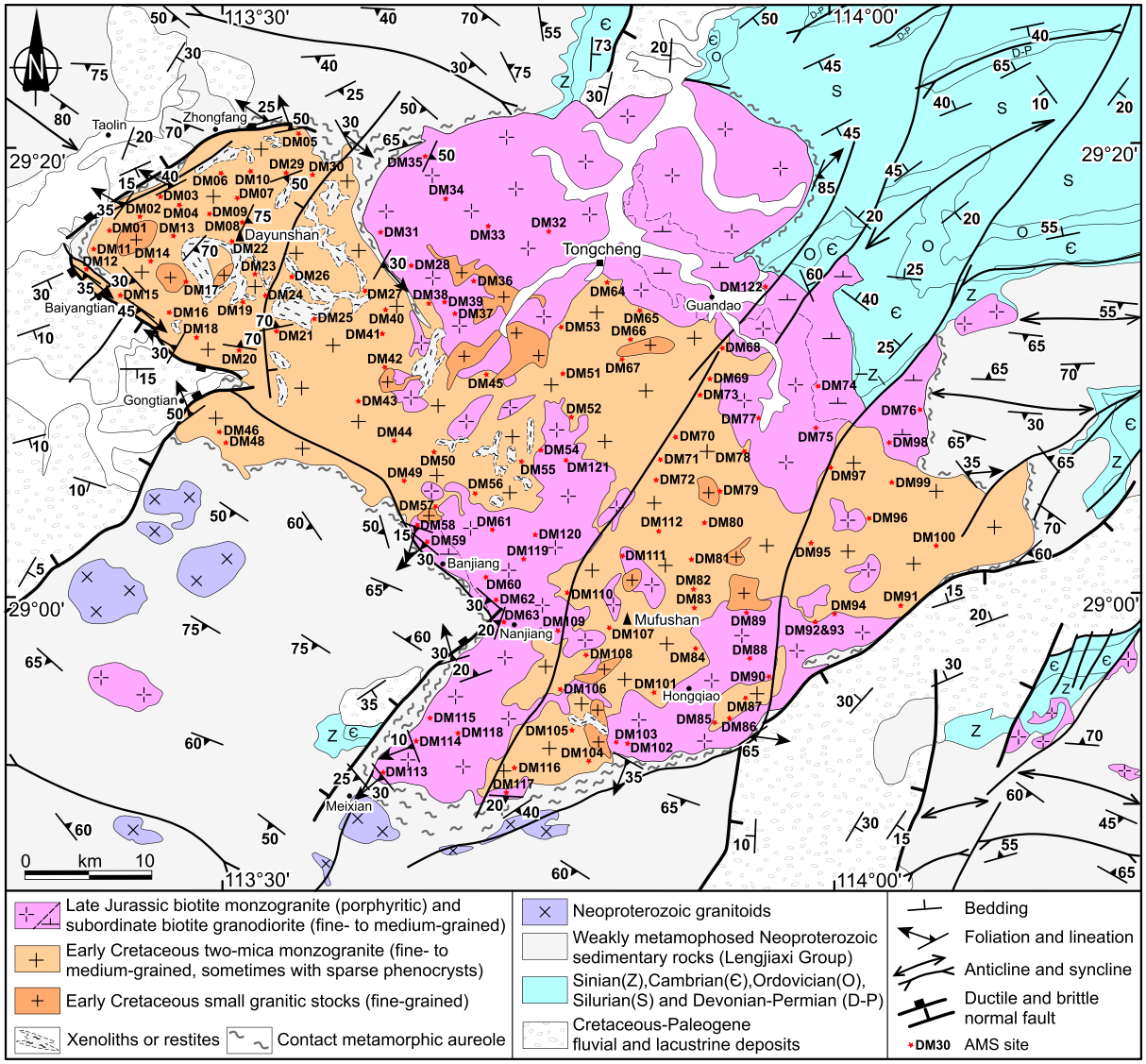

Figure 2. Geological and structural map of the Dayunshan-Mufushan area, with the sampling locations of AMS sites.

replacing biotite and plagioclase, superimposes the primary magmatic fabrics. This deuteric mineral is probably related to hydrothermal fluid activity coeval with or younger than the late-stage two-mica intrusion. The biotite granodiorite mainly occurs as a NE striking body in the northeastern part of the batholith (Guandao area, with an outcrop area of about 100 km^2). The rock is generally dark gray in color and fine- to medium-grained in texture. It has a mineral composition of plagioclase, quartz, K-feldspar, biotite, and minor hornblende. Euhedral magmatic epidote is also commonly observed. Most parts of the early-stage intrusion display typical features of isotropic granitoids (i.e., magmatic microstructures), and usually, the main granite-forming minerals do not have any particular preferred orientation. Rare mafic enclaves are locally preserved, sometimes with strongly elongated shape parallel to the magmatic foliation (Figure 3a). Along the southern wedge-shaped margin of the batholith, however, gneissic structure outlined by oriented K-feldspar megacrysts and biotite platelets is developed in the biotite monzogranite (Figures 3b and 4a). Additionally, there is a small strip (about 15 km^2) of gneissic biotite granodiorite in the southwestern margin of the batholith (Banjiang area; Figure 4b). In general, the gneissic foliation in the early-stage intrusion mainly dips to the south or SW, which sometimes exhibits a conspicuous downdip lineation (cf. Part 1). Microstructural observations

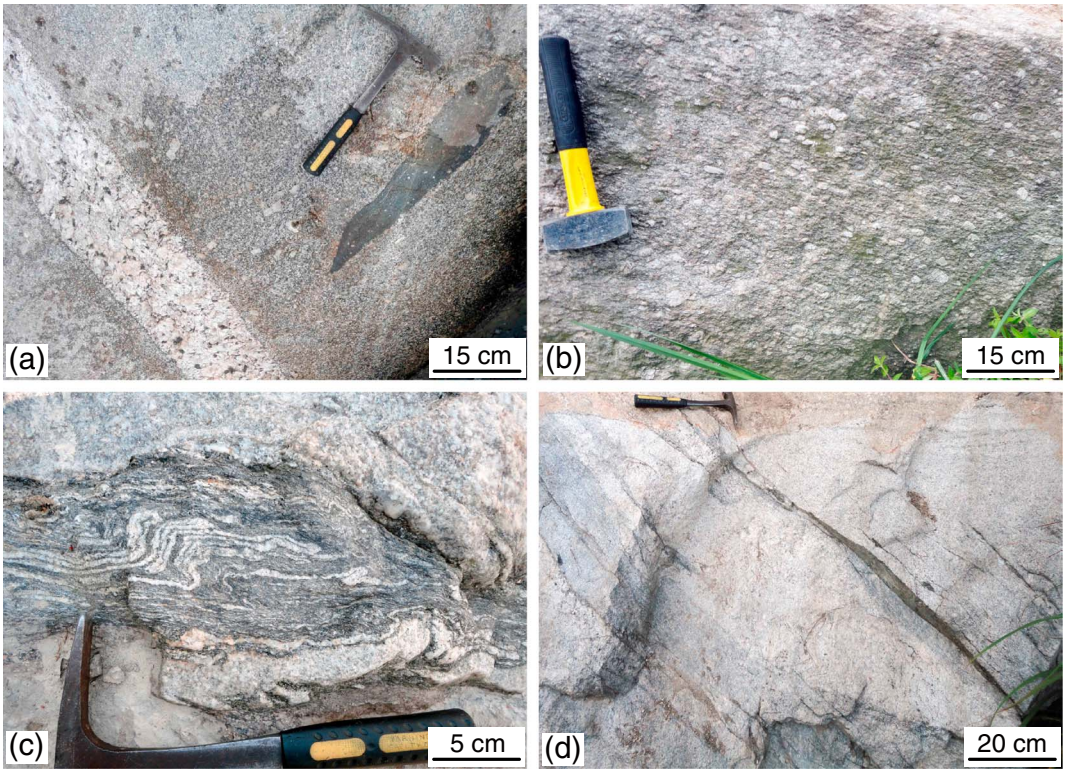

Figure 3. Field photographs of the Dayunshan-Mufushan batholith. (a) Elongated enclave in the biotite monzogranite that was cut by a pegmatite vein. (b) Porphyritic biotite monzogranite with oriented K-feldspar phenocrysts. (c) Schistose restite with synmagmatic folds in the two-mica monzogranite. (d) Outcrop of the two-mica monzogranite showing a magmatic foliation.

reveal that the gneissosity overprinted mainly under high-temperature subsolidus conditions, indicative of submagmatic to solid-state flow.

2. *A late-stage (Early Cretaceous) two-mica intrusion* composed mostly of two-mica monzogranite intruded into the early-stage intrusion generally with irregular and sharp contacts. Several kilometer-scale xenoliths of the early-stage intrusion are included in the late-stage intrusion. Except for K-feldspar, plagioclase, quartz, and biotite, primary muscovite is commonly present in the two-mica monzogranite. The rock usually exhibits a fine- to medium-grained texture, sometimes with sparse (~5% in volume) phenocrysts. Moreover, the late-stage intrusion contains a large amount of metapelitic xenoliths that were often strongly folded together with leucocratic veins (Figure 3c). Along the western tongue-shaped margin of the batholith, the Dayunshan extensional detachment fault with top-to-the-NW kinematics has been documented by our structural observations (cf. Part 1). There, the late-stage intrusion and minor metasedimentary basement in the footwall were involved in mylonitization (Figure 4c). The mylonitic granites exhibit a margin-parallel foliation with NW-SE trending lineation. A continuous transition from magmatic to solid-state flow is observed across the pluton margin. The major part of the late-stage intrusion that locally preserves well-developed magmatic foliations is characterized by widespread magmatic microstructures (Figures 3d and 4d). In addition, small stocks and leucogranitic veins intruded the aforementioned two major intrusions. The stocks mainly consist of fine-grained biotite or two-mica monzogranite, among which the largest one is about 15 km^2. The leucogranitic veins including aplite and pegmatite usually contain garnet. These rocks are generally undeformed and represent highly fractionated products formed during the final stage of the magmatic evolution.

Apart from its northeastern part that contacts with Early Paleozoic strata, the Dayunshan-Mufushan batholith chiefly intruded into the Neoproterozoic basement sequences. The batholith is surrounded by a metamorphic aureole varying from 200 m to 2 km in width. Andalusite-bearing hornfels and mica schists are

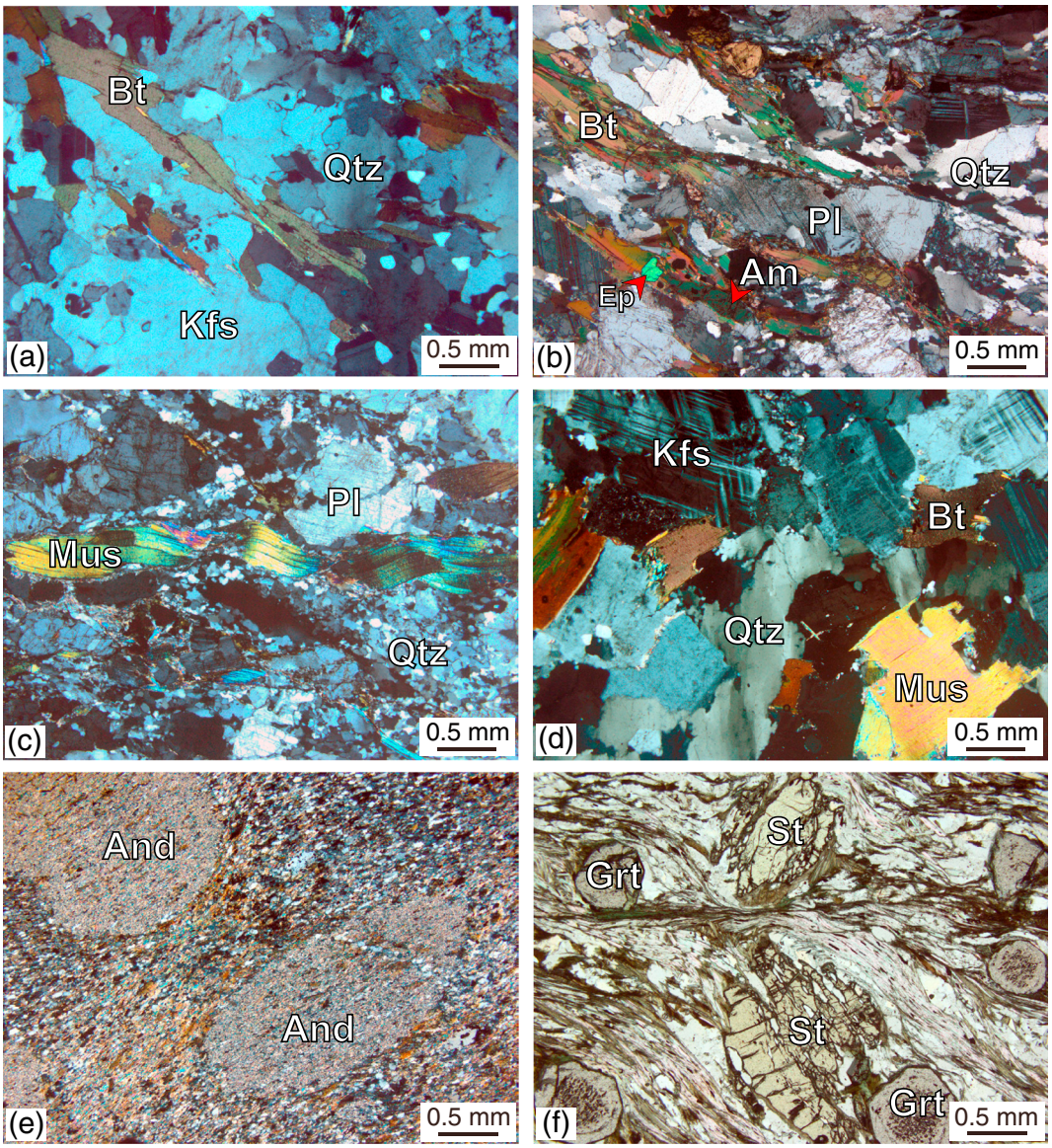

Figure 4. Petrographic and microstructural features of the Dayunshan-Mufushan batholith and its contact metamorphic rocks. (a) Biotite monzogranite with weak solid-state fabrics (slightly recrystallized quartz grains, oriented biotite) in the Meixian area. (b) Biotite granodiorite with moderate solid-state fabrics (recrystallized quartz grains, orientated biotite as well as minor amphibole) in the Banjiang area. (c) Two-mica monzogranite with strong solid-state fabrics (highly recrystallized quartz and feldspar grains, mica showing kink bands) in footwall of the Dayunshan detachment fault. (d) Two-mica monzogranite with magmatic microstructures (mica and feldspar without obvious deformation, quartz grains showing undulose extinction) in the interior of the Dayunshan massif. (e) Andalusite slate in contact zone at the northeastern border of the batholith. (f) Staurolite-garnet-mica schist with shear bands in contact zone at the southern border of the batholith. Mineral abbreviations: Kfs, K-feldspar; Pl, plagioclase; Qtz, quartz; Bt, biotite; Am, amphibole; Ep, epidote; And, andalusite; Grt, garnet; and St, staurolite.

the common contact metamorphic rock types (Figure 4e). Particularly, coexisting porphyroblasts of garnet and staurolite have been found infrequently in the schist at some localities (Figure 4f). As documented in Part 1, kinematic analysis at the southern border of the batholith indicates that the early-stage intrusion and its contact zone recorded a top-to-the-SW ductile shearing. This early deformation event (D_1) is thought to be closely related to the emplacement of the early-stage intrusion. The second but main deformation event (D_2) is featured by ductile shearing mainly along the Dayunshan detachment fault (D_{2a}) and subsequent distributed faulting of the brittle upper crust (D_{2b}). In order to determine the ages of

pluton emplacement and polyphase deformation, we conducted U-Th-Pb and $^{40}Ar/^{39}Ar$ datings. Since the detailed descriptions have already been presented in previous papers (Ji, Lin, Faure, Chen, et al., 2017; Part 1), only the final results are given here. Our zircon U-Pb dating by secondary ion mass spectrometry shows that the early-stage and late-stage intrusions of the batholith were emplaced at 151–149 Ma and ca. 132 Ma, respectively. Moreover, one of the latest stocks within the batholith was dated at ca. 127 Ma. $^{40}Ar/^{39}Ar$ dating of two gneissic granites of the early-stage intrusion yielded ages of 123–121 Ma (one amphibole and two biotite samples), while three mylonitic granites from the Dayunshan detachment fault yielded $^{40}Ar/^{39}Ar$ ages of ca. 109 Ma (one muscovite sample) and 95–93 Ma (two biotite samples). In addition, monazite U-Th-Pb chemical dating of two mica schists from the restite and contact zone related to the late-stage intrusion yielded metamorphic ages of ca. 135 Ma and ca. 129 Ma, respectively, and the monazite in the gneissic granite of the early-stage intrusion crystallized at ca. 148 Ma. Combined with structural analysis, these geochronological constrains led us to draw the following conclusions: (1) the D_1 deformation that was coeval with emplacement of the early-stage intrusion occurred at ca. 150 Ma, (2) the ductile shearing along the Dayunshan detachment initiated at ca. 132 Ma and lasted until ca. 95 Ma, and (3) the early-stage intrusion had been largely reheated due to the emplacement of the late-stage intrusion, resulting in $^{40}Ar/^{39}Ar$ age resetting of the former intrusion. Considering the regional tectonic framework, we suggested that the D_1 deformation was probably assisted by far-field compression from the northern Yangtze foreland belt. Conversely, the D_2 event represents the main extensional tectonism in the study area that dominated the syntectonic emplacement and exhumation of the late-stage intrusion especially for its western part (i.e., the Dayunshan massif).

3. Magnetic Fabrics

Based on structural observations mostly concentrated at the southern and western borders of the Dayunshan-Mufushan batholith, we identified two deformation events related to its emplacement and subsequent exhumation (cf. Part 1). However, the interiors of the batholith do not usually show mesoscopic planar and linear structures. This impedes our understanding of the pluton emplacement process and may mislead its tectonic interpretation. The AMS method is a powerful tool to reveal the structural elements of apparently isotropic to weakly deformed rocks, especially the massive granitic plutons (e.g., Améglio, Vigneresse, & Bouchez, 1997; Aranguren et al., 2003; Borradaile & Henry, 1997; Bouchez, 2000; Charles et al., 2012; Gébelin et al., 2006; Hrouda, 1982; Joly et al., 2009; Liang et al., 2015; Lin, Charles, et al., 2013; Talbot et al., 2005; Tarling & Hrouda, 1993; Turrillot et al., 2011; Wei et al., 2016; Zhang et al., 2008). Therefore, complementary to the classical structural analysis, the AMS technique has been employed to depict the fabric patterns of the Dayunshan-Mufushan batholith.

3.1. Sampling and Measurements

Considering the outcrop conditions, we tried to design the AMS sites with a relatively homogeneous spatial distribution. Unfortunately, fresh rocks are poorly exposed in the northern part of the batholith due to the intensive weathering. Finally, AMS sampling was performed at 121 sites (DM1 to DM122, with the omission of DM47) within the entire batholith (Figure 2). More than five individual cores with lengths of about 3–6 cm were sampled at each site with a portable gasoline drill. All the cores were oriented with magnetic compass in the field and, when possible, solar compass as well. An average magnetic declination of about −4° has been accordingly applied for correction. These cores were cut into standard specimens with a diameter of 2.5 cm and a length of 2.2 cm. Consequently, at least five specimens were obtained for each site, making totally 854 specimens for all the sites.

The bulk magnetic susceptibility and the anisotropy of the specimens were measured in low magnetic field, using a AGICO KLY-3S Kappabridge at the Institut des Sciences de la Terre d'Orléans (ISTO, France). The data were processed with the Anisoft 4.2 software (www.agico.com). For each site including a group of specimens, the site-average directions of the three principal axes of the AMS ellipsoid ($K_1 \geq K_2 \geq K_3$) with corresponding 95% confidence level (α_{95max} and α_{95min}) were calculated using the statistics described in Jelinek (1978). Normally, the long or maximum axis (K_1) represents the magnetic lineation, while the short or minimum one (K_3) corresponds to the pole of the magnetic foliation. Two important parameters reflecting the AMS ellipsoid features have been defined (Hrouda, 1982; Jelinek, 1981; Tarling & Hrouda, 1993): (1) the corrected

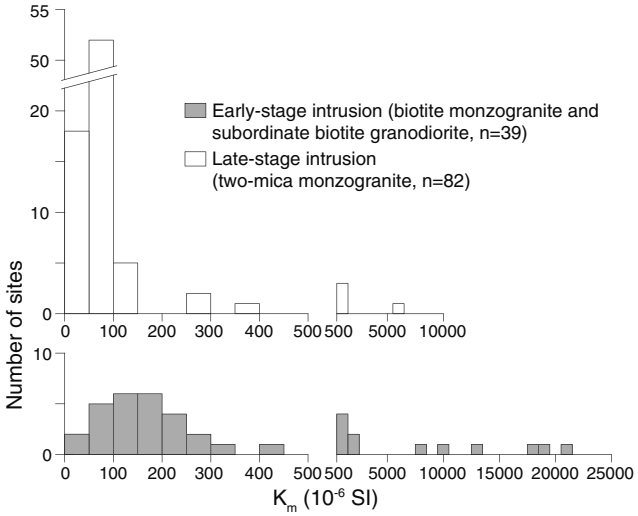

Figure 5. Histograms of mean bulk magnetic susceptibility (K_m) for the AMS sites.

anisotropy degree $P_J = \exp\sqrt{\{2[(\eta_1 - \eta)^2 + (\eta_2 - \eta)^2 + (\eta_3 - \eta)^2]\}}$ and (2) the shape factor $T = (2\eta_2 - \eta_1 - \eta_3)/(\eta_1 - \eta_3)$, varying between −1 and +1; where $\eta_1 = \ln K_1$, $\eta_2 = \ln K_2$, $\eta_3 = \ln K_3$, and $\eta = (\eta_1 + \eta_2 + \eta_3)/3$.

Identification of the mineral phases that contribute to the magnetic property is essential for all AMS studies, since the dominance of some minerals (e.g., tourmaline, cordierite, and single domain magnetite) may lead to anomalous or inverse magnetic fabrics (Borradaile & Henry, 1997; Rochette, Jackson, & Aubourg, 1992). In order to investigate the magnetic mineralogy, several methods have been used. In the laboratory of rock magnetism at ISTO, thermomagnetic experiments on rock powder were performed using the KLY-3S Kappabridge coupled with the CS3 furnace apparatus of AGICO company, while the isothermal remanent magnetization (IRM) of the representative samples was carried out by an ASC Scientific impulse magnetizer (model IM-10-30) and AGICO JR-5 spinner magnetometer. In addition, hysteresis loops were obtained by an electromagnetic inductometer at the Institut de Physique du Globe de Paris (IPGP, France).

3.2. Bulk Magnetic Susceptibility and Magnetic Mineralogy

The magnetic property of rocks is reflected by the bulk magnetic susceptibility. The mean bulk magnetic susceptibility ($K_m = (K_1 + K_2 + K_3)/3$) of each site is listed in Table S1 in the supporting information, and the histogram distribution is given in Figure 5. Most AMS sites (more than 85%) have low K_m values (<500 μSI), being in the typical range of paramagnetic granitoids (Bouchez, 2000). In detail, K_m values of the two-mica monzogranite and biotite monzogranite are mostly lower than 150 μSI and 350 μSI, respectively, indicating that paramagnetic minerals (biotite and iron-bearing muscovite) are the principal magnetic carriers. The high K_m values (>500 μSI, up to 20 mSI) are mainly from the biotite granodiorite as well as from minor two-mica or biotite monzogranites, which are due to the contribution of ferromagnetic minerals (magnetite).

Six hysteresis loops on representative samples of the different rock types were determined, revealing two types of magnetic behavior. The hysteresis curves of the two-mica and biotite monzogranites display almost perfect linear variations of the induced magnetic moment, indicating a dominance of the paramagnetic minerals (Figures 6a and 6b). In contrast, the shapes of the biotite granodiorite hysteresis loops agree with the behavior of ferromagnetic minerals with relatively large grain sizes (Figure 6c). This observation indicates that pseudo single domain to multidomain magnetite is an important magnetic carrier in the biotite granodiorite. Thermomagnetic experiments yield different types of magnetic susceptibility versus temperature curves. For the samples of two-mica and biotite monzogranites, their heating curves generally display a progressive magnetic susceptibility decrease with increasing temperatures, in agreement with the behavior of paramagnetic minerals; whereas the obvious drops at 550–600°C is attributed to the presence of magnetite (Figures 6d and 6e). The considerable raise of the cooling curves reveals that mineralogical transformations at high-temperature phase produces some new magnetite. The thermomagnetic curves of the biotite granodiorite show consistent and sharp drops of magnetic susceptibility at around 580°C, revealing the dominance of magnetite (Figure 6f). Note that the presence of thermally unstable maghemite may cause the slight drops of magnetic susceptibility at around 350°C. The IRM acquisition curves of all the measured specimens are similar, increasing rapidly below 200 mT and being almost saturated at about 300 mT (Figures 6g–6i). Such patterns confirm the presence of low-coercivity minerals such as magnetite, regardless of the plutonic rock types.

According to the above investigations, we conclude that the magnetic fabrics of the two types of monzogranites are dominated by biotite with some contribution of magnetite. For the two-mica monzogranite, muscovite may also be a significant contributor. Conversely, the biotite granodiorite can be considered as belonging to ferromagnetic granitoids (Bouchez, 2000), in which magnetite is likely an overwhelming contributor to the magnetic signal despite the presence of abundant biotite. Fortunately, there is no significant discrepancy in the subfabric orientations of phyllosilicate minerals and magnetite (Archanjo, Launeau, & Bouchez, 1995; Martín-Hernández & Hirt, 2003). Inverse magnetic fabrics are not expected in our samples due to the negligible abundance of fine-grained magnetite (single domain particles) and the absence of

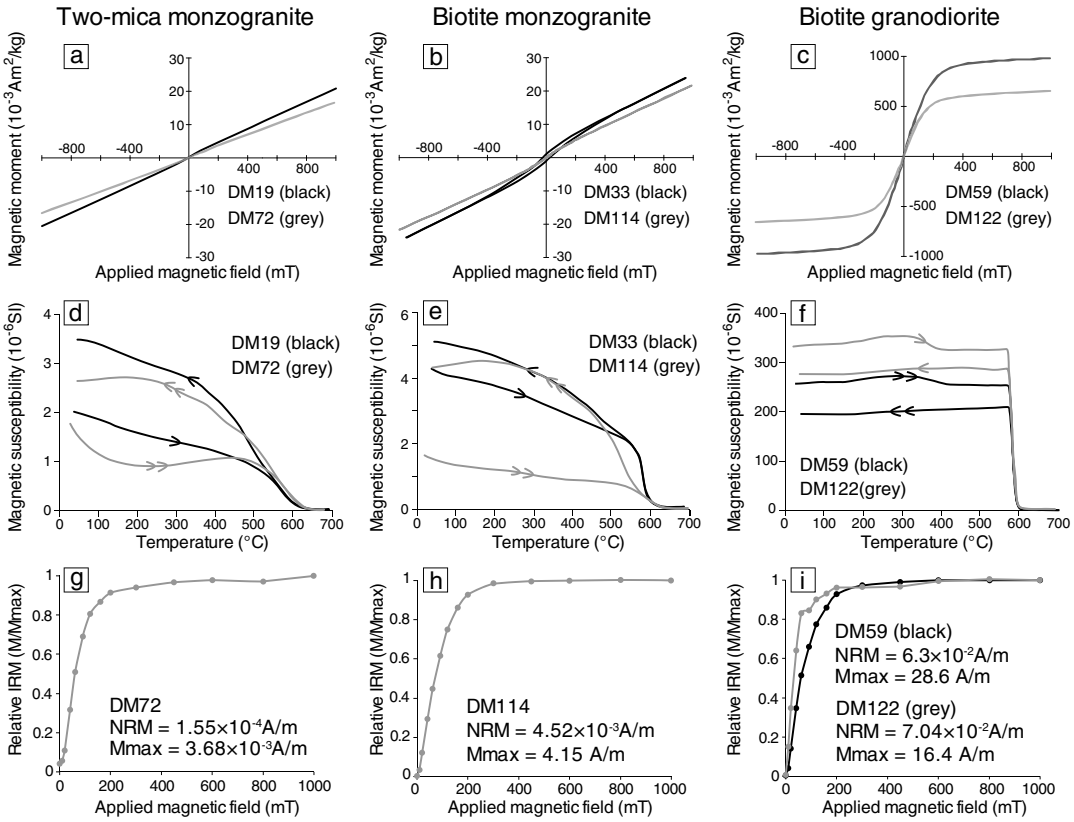

Figure 6. Magnetic mineralogy investigations of different rock types from the Dayunshan-Mufushan batholith. (a–c) Hysteresis loops, (d–f) thermomagnetic curves, and (g–i) acquisition of isothermal remanent magnetization (IRM).

tourmaline and cordierite (Borradaile & Henry, 1997; Rochette, Jackson, & Aubourg, 1992). As a consequence, K_1 and K_3 measured in this study can be confidently correlated with the magnetic lineation and the pole of the magnetic foliation, respectively.

3.3. AMS Results

The AMS data of the Dayunshan-Mufushan batholith are presented in Table S1. The parameter P_J is associated with the preferred orientation of magnetic minerals and thus can be experientially regarded as a strain intensity indicator. P_J values for most of AMS sites (>95%) are less than 1.2, with a peak at around 1.06 (Table S1 and Figures 7a and 7c). This is consistent with our field and laboratory observations that the batholith interior is dominated by magmatic fabrics due to magma flow rather than postsolidus deformation (cf. Part 1). Only a few AMS sites have high P_J values (>1.2), coming mainly from the pluton margins with gneissic structure (DM58, DM59, DM62, DM113, and DM117) or from the undeformed biotite granodiorite with high K_m values (i.e., enriched in magnetite, DM98 and DM122). The batholith margins as well as the contacts between the two major intrusions seem to have relatively high P_J value due to strain increase related to a border effect. The parameter T is used to qualify the shape of AMS ellipsoid, namely, prolate when $T < 0$, or oblate when $T > 0$. More than 85% of the sites display positive T values, indicating a dominance of the oblate ellipsoids (Table S1 and Figures 7b and 7c). This suggests that the planar fabric is statistically better defined in comparison with the linear fabric. No obvious relationship between P_J and T (Figure 7c), nor between P_J or T and K_m is observed (Figures 7a and 7b). In brief, the variations of P_J and T are independent and not significantly influenced by susceptibility discrepancies.

Equal-area projections (lower hemisphere) of the three principal axes and their site mean directions with confidence ellipses for each AMS site are presented in Figure 8, including 39 sites in the early-stage intrusion (Figure 8a) and 82 sites in the late-stage intrusion (Figure 8b). If the confidence level (α_{95}) of a magnetic axis is larger than 25°, this magnetic axis is considered to be poorly defined, and thus, its direction is not reliable. More than 75% of the AMS sites contain at least one well-defined (i.e., $\alpha_{95} \leq 25°$) magnetic axis referring to the

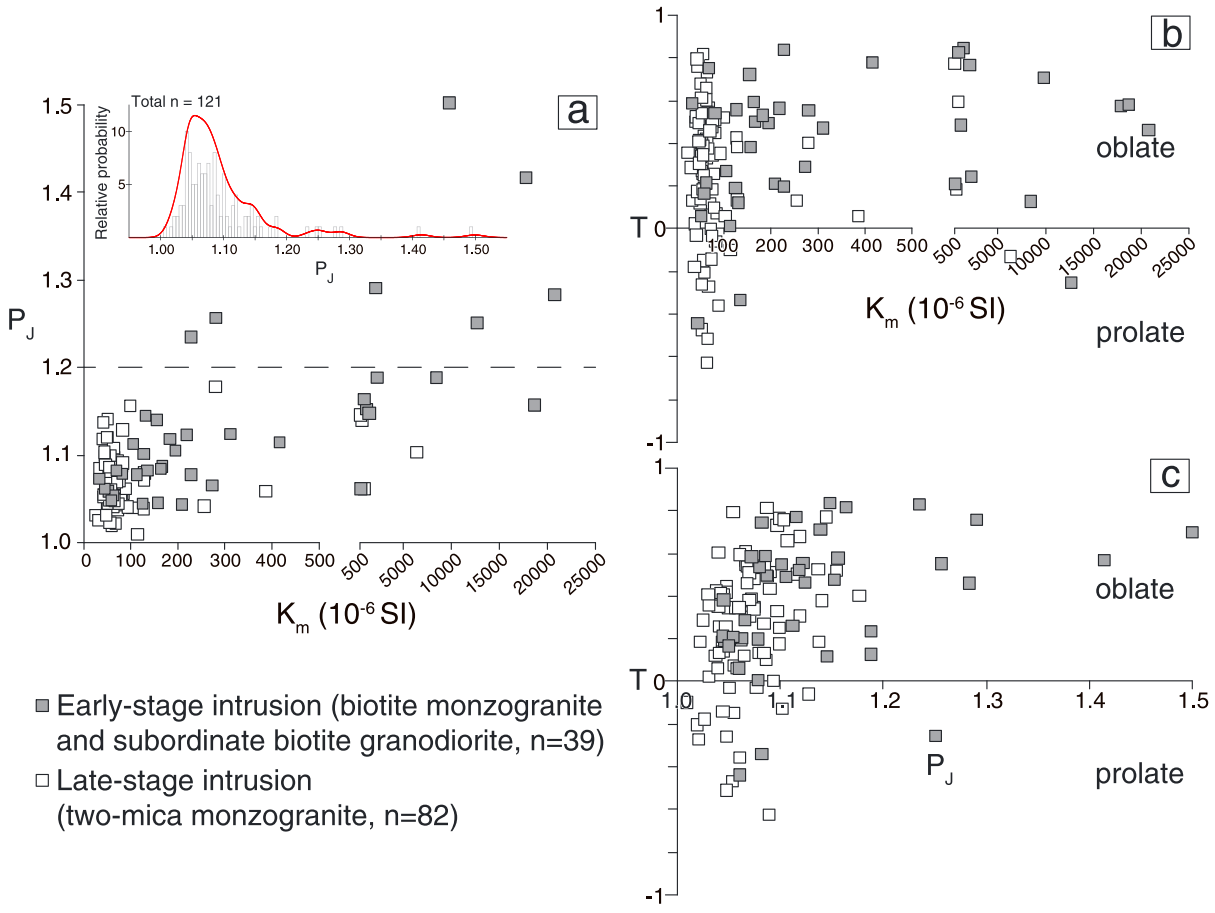

Figure 7. Relations between the AMS scalar parameters for the AMS sites. (a) T versus P_J, (b) T versus K_m, and (c) P_J versus K_m. T: shape factor, P_J: corrected anisotropy degree, and K_m: mean bulk magnetic susceptibility in 10^{-6} SI.

K_1 or K_3 (Table S1 and Figure 8). The magnetic foliations and lineations in the Dayunshan-Mufushan batholith are presented in Figure 9. The well-defined and poorly defined fabrics are shown on the maps with distinct symbols along with the stereonets of their statistical results. The fabric patterns with respect to the two major intrusions of the batholith are described as follows:

1. *Early-stage intrusion (biotite monzogranite and subordinate biotite granodiorite)*. Due to the poor outcropping conditions, the AMS sites in the northern part of the biotite monzogranite are mainly concentrated to the west of the Tongcheng city. There, the magnetic foliations strike subparallel to the pluton boundary and dip inward at moderate to high angles. Only four sites are collected from the biotite granodiorite to the east. Three of them near the contacts have subvertical foliations, while the one in the center (DM122) is nearly flat lying. The magnetic lineations in the northern part of the early-stage intrusion are ill defined, displaying NE-SW or nearly N-S trends. The southern part of the early-stage intrusion has mainly south to SW dipping foliations at gentle to moderate angles (mostly at 20°–50°), and the magnetic lineations generally plunge downdip. As for the gneissic granitoids at the southern border of the batholith, the magnetic fabrics are generally consistent with the mesoscopic structures observed in the field (cf. Part 1). It is noteworthy, however, that a few sites (e.g., DM58, DM59, and DM115) in the southern part show considerable discrepancy between the AMS and field measurements, especially for the lineation that shows a nearly W-E trend. This may be either due to the weakly inclined foliation or an overprint by the late-stage tectonomagmatism.
2. *Late-stage intrusion (two-mica monzogranite)*. The tongue-shaped Dayunshan massif is rooted in the east as revealed by gravity data (see below). Inside the pluton, the magnetic fabrics are somewhat scattered, probably as a consequence of the presence of abundant wall rock xenoliths that occupy about ~10% of the exposed surface. There, moderately to highly inclined foliations are predominant, mainly dipping to

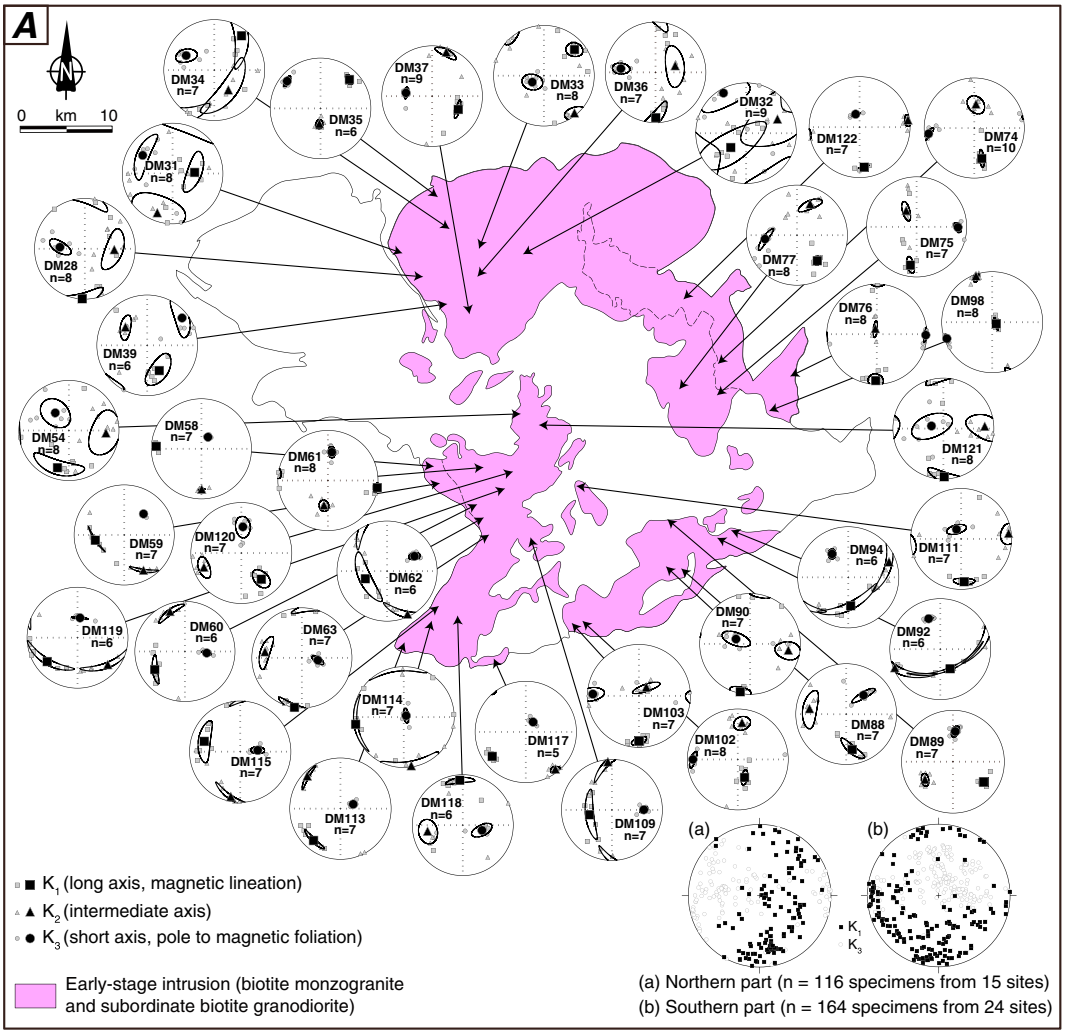

Figure 8. Equal-area projections (lower hemisphere) of the AMS results for each site in the (a) early-stage and (b) late-stage intrusions. Small gray and large black symbols (square: K_1, long axis or magnetic lineation; triangle: K_2, intermediate axis; and circle: K_3, short axis or pole to magnetic foliation) represent individual specimen and site mean direction, respectively. Confidence ellipses at 95% level are drawn around the site mean direction. Furthermore, statistical results of the K_1 and K_3 from different parts of the intrusion are also plotted.

the SE or SW. The corresponding lineation trends vary from nearly E-W to NNW-SSE. In the eastern part of the late-stage intrusion, the majority of the AMS sites have weakly inclined foliations with variable strikes, whereas the magnetic lineations cluster around a well-defined WNW-ESE direction (e.g., DM53, DM65–DM67, DM70, DM71, DM78, DM80, DM83, and DM96), subparallel to those recognized along the Dayunshan detachment to the west (cf. Part 1). A few NE-SW trending magnetic lineations are also present in the southern corridor (Mufushan area) where the late-stage intrusion has irregular contacts with the early-stage intrusion. We acknowledge, however, that it is sometimes difficult to distinguish in the field the two major intrusions when the monzogranite not only displays a porphyritic texture but also contains muscovite.

4. Gravity Survey

To detect the geological features at depth of the batholith, such as thickness variations and possible feeder zones, geophysical data are needed. Gravity survey has been proven as an efficient method to estimate the shape of granitic plutons (Améglio, Vigneresse, & Bouchez, 1997; Aranguren et al., 2003; Charles et al., 2011;

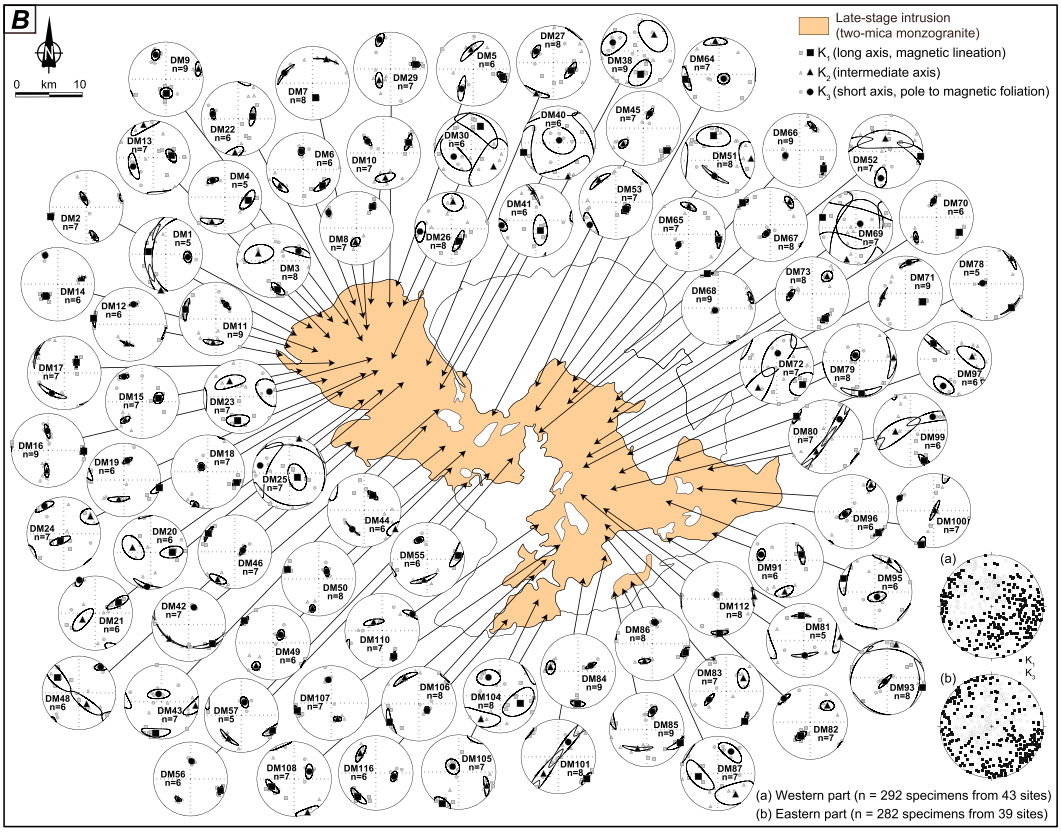

Figure 8. (continued)

Gébelin et al., 2006; Joly et al., 2009; Liang et al., 2015; Lin, Charles, et al., 2013; Talbot et al., 2005; Turrillot et al., 2011; Vigneresse, 1995; Wei et al., 2016). In this study, gravity map interpretation and two-dimensional (2-D) gravity modeling along two newly surveyed profiles have been performed.

4.1. Gravity Map Interpretation

Available gravity data from a previously regional gravity survey (1:500,000) in the study area have been collected to produce a Bouguer anomaly map (Figure 10). By comparing the gravity contours to the geological boundaries, the lower Bouguer anomalies more or less correlate with the Dayunshan-Mufushan batholith. The overall decrease of the gravity gradient toward the west and southwest indicates that the batholith becomes thinner toward these directions. In the Dayunshan massif, the gravity isocontours are strongly oblique to the pluton boundary, indicating that this tongue-shaped pluton is underlain by a thick, high-density basement sequence. By contrast, to the north and east, the isocontours are roughly parallel to the batholith borders, in agreement with the sharp contacts between the batholith and its country rocks. Some deflection of the isocontours beyond the contacts is likely related to the outward expansion of the batholith below its cover rocks. The two obvious first-order negative anomalies located in the north and east of the batholith are considered as being chiefly due to the early-stage and late-stage intrusions of the batholith. However, due to the slight density contrasts (Table S2), the precise geometry of the two major intrusions can hardly be deduced from the Bouguer anomaly map.

4.2. Gravity Profiles

In order to image with more details the geometry of the two major intrusions, two gravity profiles containing 176 stations have been realized, subparallel to the long axes of the batholith (Figure 10). The stations are spaced by ~1.5 km and ~500 m for the segments crossing the batholith borders. Precise geographic coordinates (longitude/latitude) and elevation at each station were measured using a Magellan Promark3 d-GPS system. Gravity data were collected using a Scintrex CG-5 gravimeter, and at least three measurements

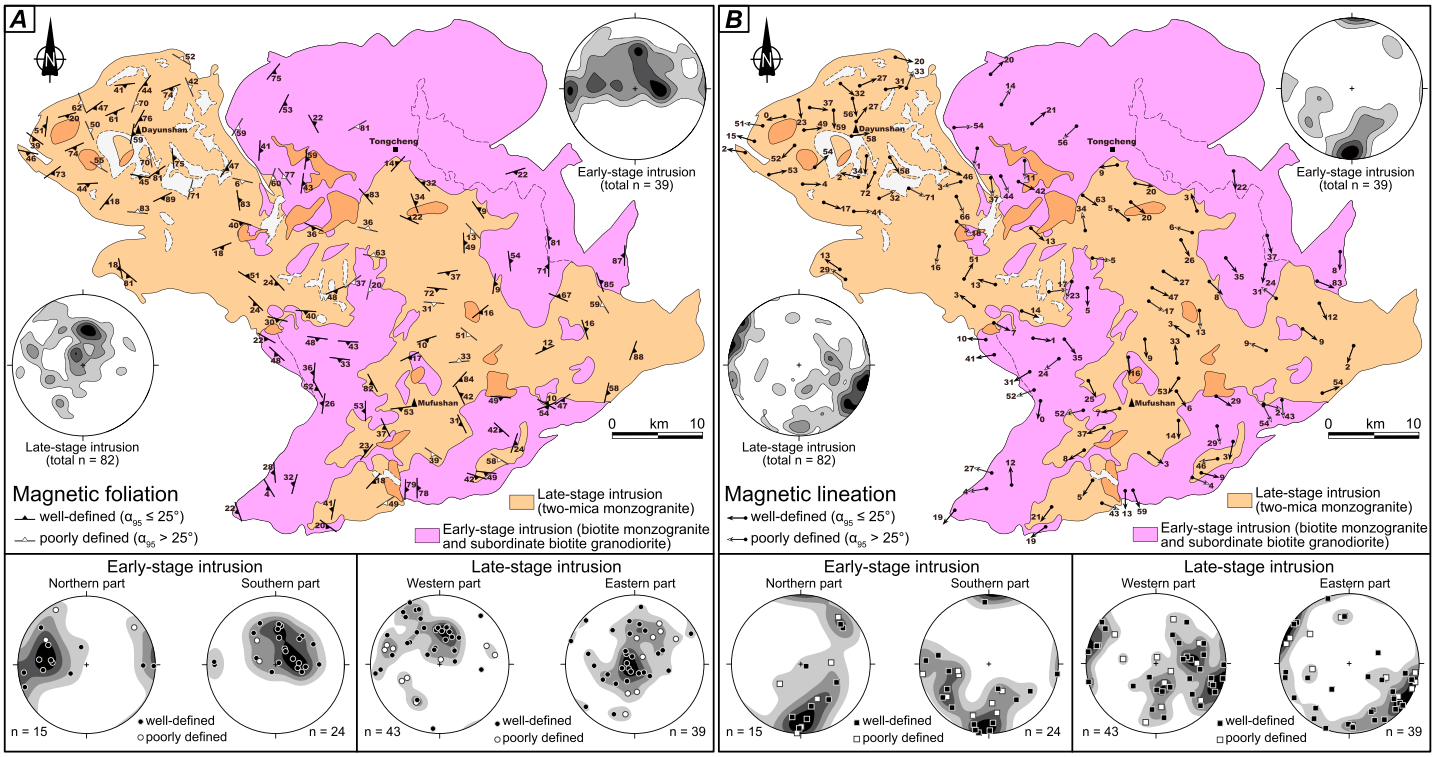

Figure 9. Magnetic fabric patterns of the Dayunshan-Mufushan batholith: (a) magnetic foliations and (b) magnetic lineations. The stereonets show the density contours of foliation poles or lineations.

were made at each station to ensure a repeatability of the measurements less than 5 μgal. During the whole period of survey, a reference station (29.265°N, 113.818°E; 111.9 m) was fixed in the Tongcheng city. The gravity anomaly was computed with respect to the theoretical value of *g* on the GRS-1967 ellipsoid. To obtain the complete Bouguer anomaly, standard free air, plateau, and terrain corrections were successively performed. A Bouguer reduction density of 2.60 g/cm^3 was chosen, close to the density of studied granitic rocks. Inner terrain corrections within a radius of 50 m for each station were estimated in the field, using the Hammer (1939) charts; outer terrain corrections up to 167 km were computed according to the procedure described in Martelet, Debéglia, and Truffert (2002).

To build a realistic gravity model, it is necessary to take into account the density contrasts between the batholith and the surrounding rocks. In the Dayunshan-Mufushan area, several geological units have been distinguished and their average densities have been estimated according to regional survey reports and our laboratory measurements (Table S2): (1) 2.59 g/cm^3 and 2.61 g/cm^3, respectively, for the Late Jurassic and Early Cretaceous intrusions (predominately biotite and two-mica monzogranites), 2.68 g/cm^3 for the subordinate granodiorite of the early-stage intrusion and the Neoproterozoic granodiorite plutons (Meixian area; Figure 2); (2) 2.73 g/cm^3 for the Neoproterozoic basement sequences as well as the larger wall rock xenoliths within the batholith; (3) 2.65 g/cm^3 for the undifferentiated pre-Mesozoic sedimentary cover (mainly the Paleozoic strata); and (4) 2.55 g/cm^3 for the Cretaceous-Paleogene continental red beds. Gravity modeling has been performed using the GM-SYS in Oasis montaj platform (www.geosoft.com). In order to simplify the modeling, we presumed that the deep crustal structure is homogeneous (with a density of 2.95 g/cm^3 below the depth of 15 km) and that the Moho surface is flat (~32 km). During the modeling process, the geometry of considered geological units with fixed densities had been adjusted to reach a good fit between measured and calculated gravity values. Meanwhile, the available geological information from maps and field observations has been taken into account for the final models (Figure 11).

Profile A is NNE-SSW trending with a length of about 80 km (Figure 11a). A negative gravity anomaly located in the northern segment of this profile corresponds to the deepest root of the early-stage intrusion, with a

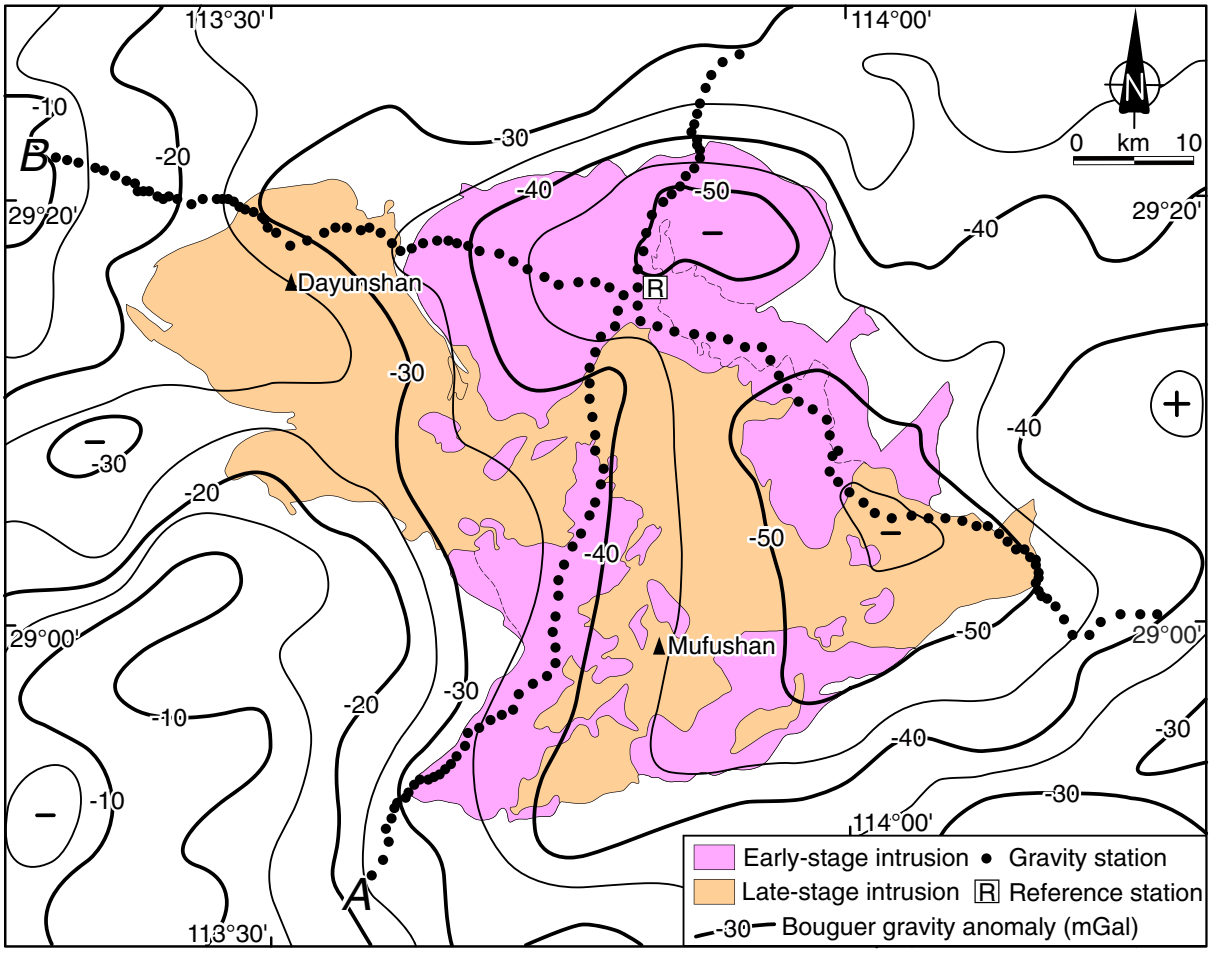

Figure 10. Bouguer anomaly map of the Dayunshan-Mufushan area. The arrays of black dots trace the two gravity profiles in Figure 11.

maximum thickness around 7 km. In the southern segment of this profile, the whole batholith exhibits a tabular shape of 2–3 km in thickness on top of the Neoproterozoic basement, while the early-stage and late-stage intrusions occur as two stacked sheets. The WNW-ESE trending profile B is about 100 km in length (Figure 11b). This profile reveals a more complex structure. The late-stage intrusion in the eastern segment of this profile shows an irregular floor characterized by considerable variations in thickness (amplitude up to 3–5 km). Considering the features of the regional gravity field, we suggest that such a geometry might extend laterally (i.e., perpendicular to the profile). Accordingly, several alternating deeper zones trending NNE-SSW can be inferred and interpreted as feeder zones for the late-stage intrusion, similarly to the observations coming from granitic plutons emplaced during crustal extension facilitated by the opening of large-scale tension gashes (Améglio, Vigneresse, & Bouchez, 1997; Talbot et al., 2005; Turrillot et al., 2011; Vigneresse, 1995; Wei, Martelet, et al., 2014). Toward the Dayunshan massif, the late-stage intrusion partly extends beneath the early-stage intrusion and exhibits a laccolitic body. Several large xenolithic blocks of metasedimentary rocks have been inferred in this massif according to our modeling. It is assumed that the Dayunshan detachment fault is westward dipping and becomes listric at depth. In addition, profile B also cuts across the two half grabens on both sides of the batholith. The accumulation of alluvial deposits in the southeastern basin reaches 2 km in thickness.

5. Emplacement Modes and Their Bearings on the Regional Tectonics

The combination of the AMS and gravity data makes possible the recognition of hidden structures that are invisible by field observations. Such a combined approach has already been successfully applied to

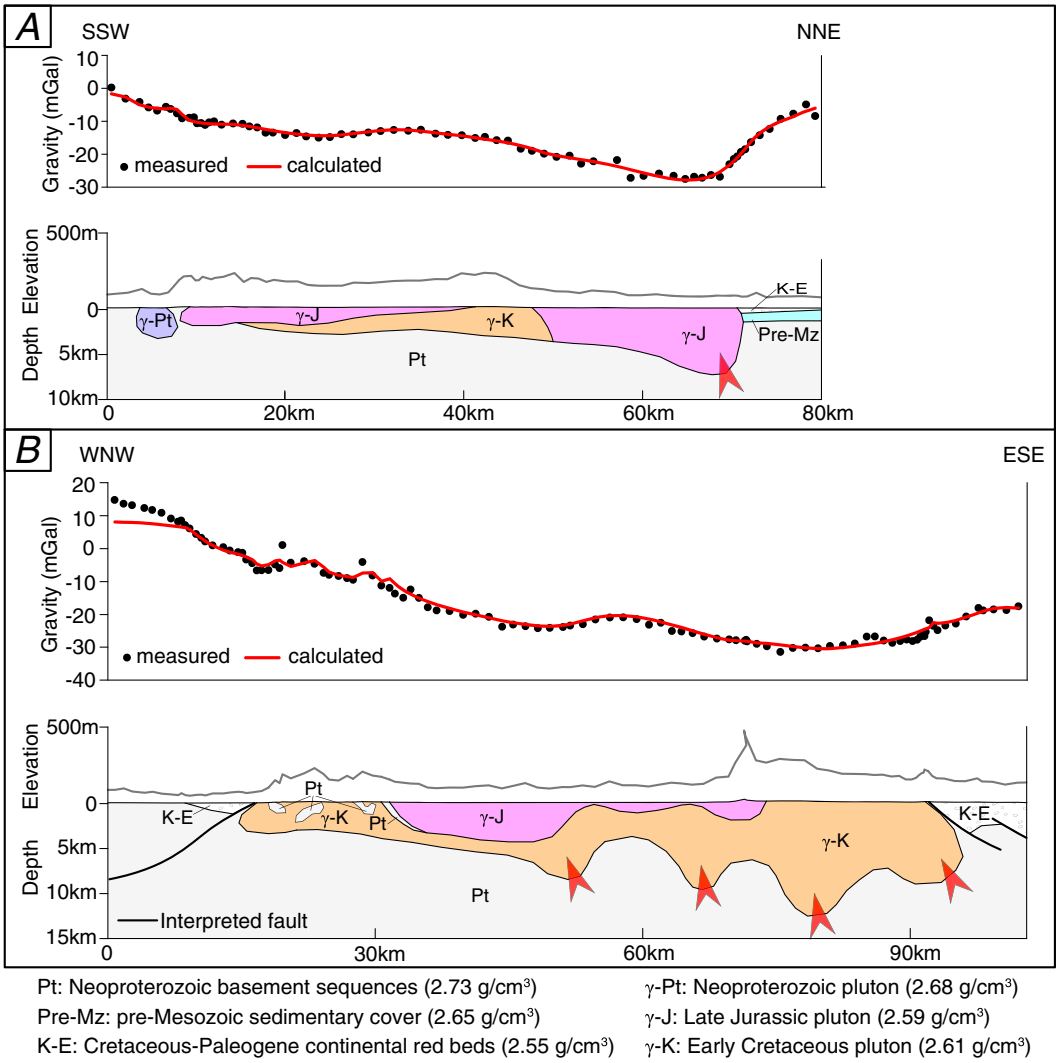

Figure 11. Forward gravity modeling along (a) NNE-SSW and (b) WNW-ESE trending profiles across the Dayunshan-Mufushan batholith. Note that the arrow shows the possible feeder zone for the pluton.

decipher the pluton emplacement modes, such as in the European Variscan belt (e.g., Améglio, Vigneresse, & Bouchez, 1997; Aranguren et al., 2003; Gébelin et al., 2006; Joly et al., 2009; Talbot et al., 2005; Turrillot et al., 2011), as well as in eastern China (Liang et al., 2015; Lin, Charles, et al., 2013; Wei et al., 2016). Fabric patterns in granitic plutons can be attributed to magma flow, solid-state deformation, or a combination of both processes (e.g., Bouchez, 2000; Paterson et al., 1998). As described before, solid-state fabrics (gneissic or mylonitic structures) are only developed along the southern and western margins of the Dayunshan-Mufushan batholith, whereas magmatic microstructures without obvious mesoscopic deformation dominate inside the batholith. Thus, the magnetic fabrics collected in this study were mainly acquired during or just after the full crystallization of the magma. This conclusion is confirmed by our microstructural observations and by the low P_J values for most of the AMS sites (Figure 7). The magnetic lineation patterns in the batholith define two maxima oriented NNE-SSW (mean at 190°/29°) and WNW-ESE (mean at 117°/20°) for the early-stage and late-stage intrusions, respectively (Figure 9). These two groups of magnetic lineations are consistent with the tectonic ones, namely, L_1 of the D_1 deformation at ca. 150 Ma and L_2 of the D_2 deformation during 132–95 Ma (cf. Part 1). This suggests that the fabric patterns of the two major intrusions were probably influenced by distinct stress fields during their emplacement, implying that their emplacement modes and corresponding tectonic significance would be different.

Although our coverage of the AMS sites in the northern part of the early-stage intrusion is rather sparse, the magnetic foliations therein appear to display a concentric arrangement. Such a situation is usually considered as a consequence of magma inflation above a main feeder zone. Moreover, this inference agrees with the gravity data that show the deepest root of the early-stage intrusion is located in the north (Figures 10 and 11). It is conceivable that the geometry of the early-stage intrusion, prior to its breakup, would be tear shaped in horizontal section and wedge shaped in vertical section, with a thickness decreasing toward the southern tip. Accordingly, we contend that the magma was fed from sources below the northern part of the early-stage intrusion and then spread southward at shallow depths. The overall direction of magma transport, subparallel to the nearly N-S to NE-SW oriented magnetic lineations, is compatible with the top-to-the SW shearing at the southern border of the batholith. Conversely, for the late-stage intrusion, the gravity modeling draws an inference of several linear feeder zones (Figure 11). They likely correspond to extensional fractures created by a NW-SE stretching. Weakly inclined foliations are predominant in the eastern part of the late-stage intrusion, which might be due to flattening against the pluton roof. The well-grouped lineations in this part of the pluton, mostly trending around the WNW-ESE, are explained by lateral magma expansion above the multiple feeder zones. Finally, the Dayunshan massif appears in the west as a laccolitic body. We suggest that it was stretched from the east, largely due to the activity of the Dayunshan detachment fault.

In the light of the above AMS and gravity modeling results, combined with previous structural and geochronological data of Part 1, a scenario is proposed for a two-stage construction of the Dayunshan-Mufushan batholith. During the first stage (ca. 150 Ma), partial melting of the deep crust generated the early-stage magma. The magma was injected vertically through a main feeder zone. Far-field compression from the north (the D_1 event) facilitated a southward expansion of the magma during its ascent and emplacement. Consequently, a top-to-the-SW ductile shearing was developed along the southern margin of the early-stage intrusion when the magma approached its complete crystallization. During the secondary stage, the study area was affected by a regional NW-SE extension (the D_2 event), and the crustal meting generated the late-stage magma. The ascending magma was gathered through several NNE-SSW trending feeder zones almost perpendicular to the regional stretching direction. Above these feeder zones, the magma expanded mainly along the WNW-ESE direction and eventually formed a single pluton. During this process, the early-stage intrusion had been broken up and partly recycled into the late-stage magma. Coeval with magma emplacement and crystallization, the top-to-the-NW Dayunshan detachment to the west began to be activated due to strain localization. Later, about 127 Ma, small stocks of magma batches intruded into the early-stage and late-stage intrusions.

6. Geodynamic Setting

Two major magmatic flare-up events took place in southeast China during the Late Mesozoic, respectively, at ca. 165–150 Ma and ca. 140–90 Ma, whereas the interval appears to be a period of "magmatic quiescence" (Ji, Lin, Faure, Chen, et al., 2017; X. H. Li et al., 2010; Liu et al., 2012; Wu et al., 2012). As yet the subduction of the paleo-Pacific (i.e., Izanagi) Plate beneath the SCB that initiated at least before the Middle Jurassic has been considered as the most plausible geodynamic trigger responsible for the Late Mesozoic magmatic activity. For instance, Zhou and Li (2000) argued for a change in slab dip angle of the paleo-Pacific Plate from a very low to a medium angle during the period from 180 to 80 Ma, accounting for the apparently oceanward younging trend of the magmatic activity. Instead, Li and Li (2007) proposed a flat subduction to interpret the Early Mesozoic intracontinental tectonics and associated magmatism in the inland of south China. They also suggested that the Jurassic magmatism was caused by foundering of the subducted oceanic flat slab. There is a broad consensus that the Cretaceous magmatism was related to slab rollback of the paleo-Pacific Plate (Ji, Lin, Faure, Chen, et al., 2017; Jiang et al., 2011; Li & Li, 2007; Liu et al., 2012; Wong et al., 2009). In particular, an asynchronous rollback has been proposed based on systematical investigation of the Cretaceous volcanism in southeast China coastal region (L. Liu, Xu, & Xia, 2016).

We favor the proposal that a Jurassic slab foundering and a Cretaceous slab rollback best explain the Late Mesozoic tectonomagmatism in the SCB. Considering the far distance between the magmatic front and the paleo-Pacific trench, the foundered slab during the Jurassic might be continental lithosphere resulting from the Triassic intracontinental subduction in the central SCB (see Ji, Lin, Faure, Chen, et al., 2017, for a discussion). The geochemical features of the Jurassic magmatic rocks in southeast China argue for an intraplate

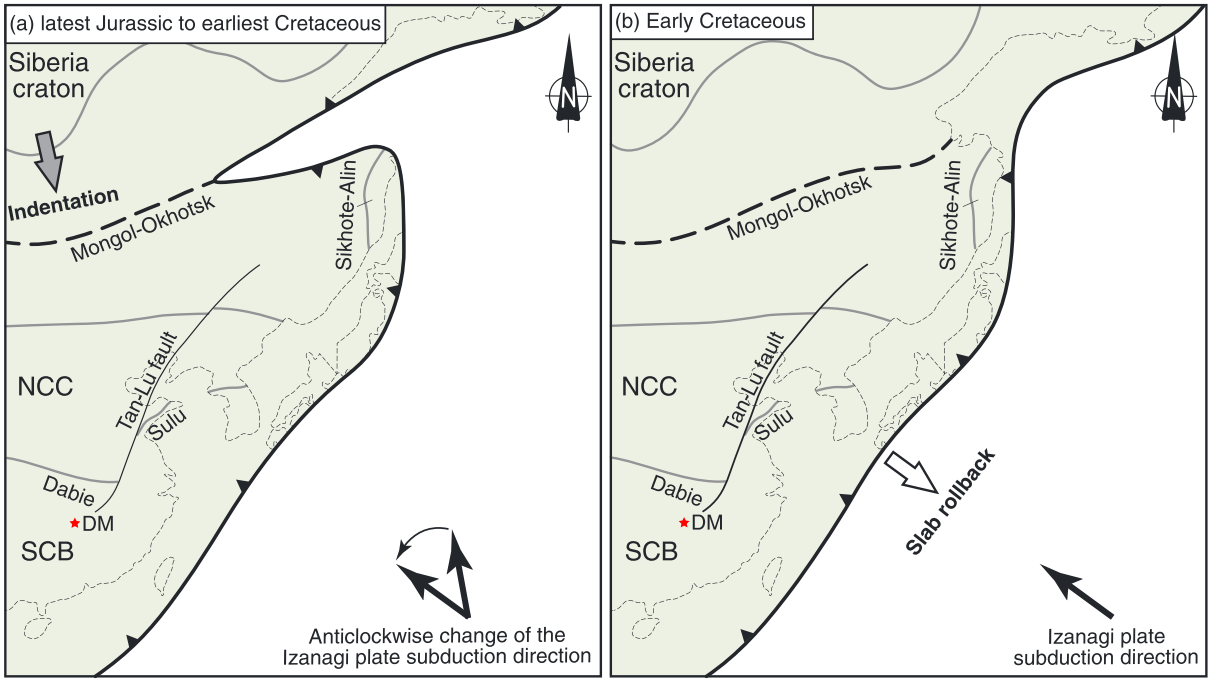

Figure 12. Geodynamic setting of East Asia during the Late Mesozoic. According to recent global plate reconstructions (Müller et al., 2016; Seton et al., 2012), the subducted plate along the eastern Asian continental margin prior to the Cenozoic was mostly the Izanagi Plate rather than the Pacific Plate. It is estimated that the Pacific Plate was born in the Early Jurassic at a triple junction surrounded by the Izanagi, Farallon, and Phoenix Plates, and the Izanagi-Pacific ridge subduction occurred at ca. 60–55 Ma. Following the closure of the Mongol-Okhotsk Ocean with doubly vergent subduction during the latest Jurassic to earliest Cretaceous (Cogné et al., 2005; Van der Voo et al., 2015; Yang et al., 2015), the Izanagi Plate probably experienced a change from oblique to orthogonal subduction. Subsequently, the subducted Izanagi slab started to stagnate in the mantle transition zone beneath the eastern Asian continent due to its slab rollback, similar to the present situation of the subducting Pacific slab as revealed by seismic tomography (Huang & Zhao, 2006; Liu et al., 2017). The red star marks the location of the Dayunshan-Mufushan batholith (DM).

extensional setting (Huang et al., 2013, 2015; Li et al., 2007). Slab foundering can induce substantial basaltic underplating, leading to crustal melting for the generation of felsic magmatism. Such a process is in agreement with the observation that most of the Jurassic plutons in the inland area (e.g., Nanling Range) display anorogenic features. Usually, no large-scale crustal deformation coeval with emplacement can be determined in the country rocks (Feng et al., 2012; H. S. Liu et al., 2016). In other words, regional tectonics might not be a crucial factor controlling the emplacement processes of these plutons. We further infer that the "magmatic quiescence" of the SCB probably foreshadowed the geodynamic transformation from slab foundering to slab rollback of the paleo-Pacific Plate. Taking into account the distinct spatial distribution of the Jurassic and Cretaceous magmatic rocks, that is, nearly W-E trending versus NE trending, a counterclockwise change of the subduction direction during this period is likely, as suggested by Liu et al. (2012). In addition, since there would be variations of the subduction angle after the slab foundering to the south, slab tearing beneath the lower Yangtze River belt in east central China might have also occurred (Wu et al., 2012). Due to the reorganization of the paleo-Pacific subduction as well as the closure of the Mongol-Okhotsk and Bangong-Nujiang oceans, the eastern Asian continent was surrounded by multidirected convergent tectonics during the Jurassic to earliest Cretaceous (Figure 12a). Indeed, intracontinental contractional tectonics during this period has been documented in many places of eastern China, such as the development of several thrust-fold belts surrounding the Ordos and Sichuan Basins (Dong et al., 2015; Faure, Lin, & Chen, 2012; Li et al., 2012; Liu et al., 2015; Yan et al., 2003). This leads us to believe that the emplacement of the Dayunshan-Mufushan early-stage intrusion was partially assisted by a distal compressional regime as demonstrated by our multidisciplinary data (see also Part 1). It is generally considered that the Cretaceous magmatism in southeast China was induced by lithospheric extension (Li, 2000; J. H. Li et al., 2014; Wang & Shu, 2012; Zhou & Li, 2000). The synextensional emplacement of the Dayunshan-Mufushan late-stage intrusion in this study provides robust evidence to support this conclusion. Cretaceous back-arc extension triggered by episodic slab rollback must be largely responsible for the development of the southeast China basin-and-range

tectonic system (Figure 12b). Such a geodynamic case has also been considered as the best candidate for the contemporaneous destruction of the NCC (Zhu et al., 2012, and references therein). Since the Cretaceous extensional tectonics occurred throughout the eastern Asian continent from the Transbaikalia region of Russia to south China, generally characterized by a NW-SE maximum stretching direction (cf. Part 1), the effect of the paleo-Pacific subduction only cannot explain all the tectonic phenomena. This point has already been noticed by Lin, Faure, et al. (2013), yet further studies are still needed to reveal the geodynamic significance of this continental-scale extension.

7. Conclusions

A combined AMS and gravity study enable us to better understand the multiple emplacement processes of the Dayunshan-Mufushan batholith. The magnetic fabrics in the batholith interiors are dominated by magma flow, with generally low P_J values. Two maxima referring to the magnetic lineation orientations are defined, trending NNE-SSW and WNW-ESE for the early-stage and late-stage intrusions, respectively. They are consistent with the tectonic lineations, respectively, recognized at the southern and western borders of the batholith. The early-stage intrusion thins southward and its northern part is interpreted as the main feeder zone. A southward magma transport partially assisted by far-field compression from the north is suggested for emplacement of the early-stage intrusion at ca. 150 Ma. On the contrary, the late-stage intrusion emplaced during the regional NW-SE crustal stretching, with lateral magma expansion above several linear feeder zones as inferred from gravity modeling. Particularly, ductile shearing of the Dayunshan detachment during 132–95 Ma significantly exhumed the late-stage intrusion. In general, the magnetic foliations of the two major intrusions can be well explained by their contrasted emplacement modes. These new results allow us to propose a two-stage construction of the Dayunshan-Mufushan batholith with distinct tectonic regimes from compressional to extensional. In combination with tectonic reconstructions, we suggest that the "magmatic quiescence" around the Jurassic-Cretaceous boundary in southeast China probably corresponds to a contractional setting due to subduction adjustment of the paleo-Pacific Plate coeval with the final closure of the Mongol-Okhotsk Ocean, while the Cretaceous extensional tectonics and associated magmatism therein are largely related to episodic slab rollback.

Acknowledgments

Supplementary data related to this article can be found in the supporting information or are available by contacting the first author (e-mail: jiwenbin@mail.iggcas.ac.cn). This work has been financially supported by the MOST of China (grants 2016YFC0600401 and 2016YFC0600102) and the NSFC (grants 41502202 and 41225009). Special thanks are due to Guillaume Martelet in BRGM (France) for his assistance with the gravity modeling. We also thank Jean-Luc Bouchez, Jiří Žák, and Paul Tregoning (Editor) for their careful, critical and constructive reviews that have greatly helped us to improve the manuscript.

References

Améglio, L., Vigneresse, J. L., & Bouchez, J. L. (1997). Granite pluton geometry and emplacement mode inferred from combined fabric and gravity data. In J. L. Bouchez, D. H. W. Hutton, & W. E. Stephens (Eds.), *Granite: From segregation of melt to emplacement fabrics* (pp. 199–214). Dordrecht, Netherlands: Springer. https://doi.org/10.1007/978-94-017-1717-5_13

Aranguren, A., Cuevas, J., Tubía, J. M., Román-Berdiel, T., Casas-Sainz, A., & Casas-Ponsati, A. (2003). Granite laccolith emplacement in the Iberian arc: AMS and gravity study of the La Tojiza pluton (NW Spain). *Journal of the Geological Society of London*, *160*(3), 435–445. https://doi.org/10.1144/0016-764902-079

Archanjo, C. J., Launeau, P., & Bouchez, J. L. (1995). Magnetic fabrics vs. magnetite and biotite shape fabrics of the magnetite-bearing granite pluton of Gameleiras (Northeast Brazil). *Physics of the Earth and Planetary Interiors*, *89*(1–2), 63–75. https://doi.org/10.1016/0031-9201(94)02997-P

Borradaile, G. J., & Henry, B. (1997). Tectonic applications of magnetic susceptibility and its anisotropy. *Earth Science Reviews*, *42*(1–2), 49–93. https://doi.org/10.1016/S0012-8252(96)00044-X

Bouchez, J. L. (2000). Anisotropie de susceptibilité magnétique et fabrique des granites (Magnetic susceptibility anisotropy and fabrics in granites). *Comptes Rendus de l'Académie des Sciences Paris*, *330*, 1–14.

Bouchez, J. L., Hutton, D. H. W., & Stephens, W. E. (1997). *Granite: From segregation of melt to emplacement fabrics*. Dordrecht, Netherlands: Springer. https://doi.org/10.1007/978-94-017-1717-5

Brown, M. (2013). Granite: From genesis to emplacement. *Geological Society of America Bulletin*, *125*(7–8), 1079–1113. https://doi.org/10.1130/B30877.1

Bureau of Geology and Mineral Resources of Hunan Province (1988). *Regional geology of Hunan Province* [in Chinese with English abstract]. Beijing: Geological Publishing House.

Castro, A. (1987). On granitoid emplacement and related structures. A review. *Geologische Rundschau*, *76*(1), 101–124. https://doi.org/10.1007/BF01820576

Charles, N., Gumiaux, C., Augier, R., Chen, Y., Faure, M., Lin, W., & Zhu, R. X. (2012). Metamorphic core complex dynamics and structural development: Field evidences from the Liaodong Peninsula (China, East Asia). *Tectonophysics*, *560–561*, 22–50.

Charles, N., Gumiaux, C., Augier, R., Chen, Y., Zhu, R. X., & Lin, W. (2011). Metamorphic core complexes vs. synkinematic plutons in continental extension setting: Insights from key structures (Shandong Province, eastern China). *Journal of Asian Earth Sciences*, *40*(1), 261–278. https://doi.org/10.1016/j.jseaes.2010.07.006

Charvet, J., Shu, L. S., Faure, M., Choulet, F., Wang, B., Lu, H. F., & Le Breton, N. (2010). Structural development of the lower Paleozoic belt of south China: Genesis of an intracontinental orogen. *Journal of Asian Earth Sciences*, *39*(4), 309–330. https://doi.org/10.1016/j.jseaes.2010.03.006

Chen, C. H., Lee, C. Y., & Shinjo, R. (2008). Was there Jurassic paleo-Pacific subduction in south China?: Constraints from $^{40}Ar/^{39}Ar$ dating, elemental and Sr–Nd–Pb isotopic geochemistry of the Mesozoic basalts. *Lithos*, *106*(1–2), 83–92. https://doi.org/10.1016/j.lithos.2008.06.009

Chu, Y., Faure, M., Lin, W., & Wang, Q. C. (2012). Early Mesozoic tectonics of the South China Block: Insights from the Xuefengshan intracontinental orogen. *Journal of Asian Earth Sciences*, *61*, 199–220. https://doi.org/10.1016/j.jseaes.2012.09.029

Chu, Y., Faure, M., Lin, W., Wang, Q. C., & Ji, W. B. (2012). Tectonics of the Middle Triassic intracontinental Xuefengshan belt, south China: New insights from structural and chronological constraints on the basal décollement zone. *International Journal of Earth Sciences*, *101*(8), 2125–2150. https://doi.org/10.1007/s00531-012-0780-5

Chu, Y., & Lin, W. (2014). Phanerozoic polyorogenic deformation in southern Jiuling massif, northern South China Block: Constraints from structural analysis and geochronogy. *Journal of Asian Earth Sciences*, *86*, 117–130. https://doi.org/10.1016/j.jseaes.2013.05.019

Cogné, J.-P., Kravchinsky, V. A., Halim, N., & Hankard, F. (2005). Late Jurassic–early cretaceous closure of the Mongol–Okhotsk Ocean demonstrated by new Mesozoic palaeomagnetic results from the trans-Baïkal area (SE Siberia). *Geophysical Journal International*, *163*(2), 813–832. https://doi.org/10.1111/j.1365-246X.2005.02782.x

Davis, G. A., Zheng, Y. D., Wang, C., Darby, B. J., Zhang, C. H., & Gehrels, G. (2001). Mesozoic tectonic evolution of the Yanshan fold and thrust belt, with emphasis on Hebei and Liaoning provinces, northern China. *Geological Society of America Memoirs*, *194*, 171–194.

Dong, S. W., Zhang, Y. Q., Zhang, F. Q., Cui, J. J., Chen, X. H., Zhang, S. H., … Li, H. L. (2015). Late Jurassic–Early Cretaceous continental convergence and intracontinental orogenesis in East Asia: A synthesis of the Yanshan revolution. *Journal of Asian Earth Sciences*, *114*, 750–770. https://doi.org/10.1016/j.jseaes.2015.08.011

Faure, M., Lin, W., & Chen, Y. (2012). Is the Jurassic (Yanshanian) intraplate tectonics of north China due to westward indentation of the North China Block? *Terra Nova*, *24*(6), 456–466. https://doi.org/10.1111/ter.12002

Faure, M., Lin, W., Chu, Y., & Lepvrier, C. (2016). Triassic tectonics of the southern margin of the South China Block. *Comptes Rendus Geoscience*, *348*(1), 5–14. https://doi.org/10.1016/j.crte.2015.06.012

Faure, M., Shu, L. S., Wang, B., Charvet, J., Choulet, F., & Monié, P. (2009). Intracontinental subduction: A possible mechanism for the early Palaeozoic Orogen of SE China. *Terra Nova*, *21*(5), 360–368. https://doi.org/10.1111/j.1365-3121.2009.00888.x

Feng, Z. H., Wang, C. Z., Zhang, M. H., & Liang, J. C. (2012). Unusually dumbbell-shaped Guposhan–Huashan twin granite plutons in Nanling range of south China: Discussion on their incremental emplacement and growth mechanism. *Journal of Asian Earth Sciences*, *48*, 9–23. https://doi.org/10.1016/j.jseaes.2011.12.022

Gébelin, A., Martelet, G., Chen, Y., Brunel, M., & Faure, M. (2006). Structure of late Variscan Millevaches leucogranite massif in the French massif central: AMS and gravity modelling results. *Journal of Structural Geology*, *28*(1), 148–169. https://doi.org/10.1016/j.jsg.2005.05.021

Gilder, S. A., Gill, J., Coe, R. S., Zhao, X. X., Liu, Z. W., Wang, G. X., … Wu, H. R. (1996). Isotopic and paleomagnetic constraints on the Mesozoic tectonic evolution of south China. *Journal of Geophysical Research*, *101*(B7), 16,137–16,154. https://doi.org/10.1029/96JB00662

Gilder, S. A., Keller, G. R., Luo, M., & Goodell, P. C. (1991). Timing and spatial distribution of rifting in China. *Tectonophysics*, *197*(2–4), 225–243. https://doi.org/10.1016/0040-1951(91)90043-R

Hammer, S. (1939). Terrain corrections for gravimeter stations. *Geophysics*, *4*(3), 184–194. https://doi.org/10.1190/1.1440495

Hrouda, F. (1982). Magnetic anisotropy of rocks and its application in geology and geophysics. *Geophysical Surveys*, *5*(1), 37–82. https://doi.org/10.1007/BF01450244

Huang, H. Q., Li, X. H., Li, Z. X., & Li, W. X. (2013). Intraplate crustal remelting as the genesis of Jurassic high-K granites in the coastal region of the Guangdong Province, SE China. *Journal of Asian Earth Sciences*, *74*, 280–302. https://doi.org/10.1016/j.jseaes.2012.09.009

Huang, H. Q., Li, X. H., Li, Z. X., & Li, W. X. (2015). Formation of the Jurassic south China large Granitic Province: Insights from the genesis of the Jiufeng pluton. *Chemical Geology*, *401*, 43–58. https://doi.org/10.1016/j.chemgeo.2015.02.019

Huang, J. L., & Zhao, D. P. (2006). High-resolution mantle tomography of China and surrounding regions. *Journal of Geophysical Research*, *111*, B09305. https://doi.org/10.1029/2005JB004066

Hutton, D. H. W. (1988). Granite emplacement mechanisms and tectonic controls: Inferences from deformation studies. *Transactions of the Royal Geological Society of Edinburgh: Earth Sciences*, *79*(2–3), 245–255. https://doi.org/10.1017/S0263593300014255

Jelinek, V. (1978). Statistical processing of anisotropy of magnetic susceptibility measured on groups of specimens. *Studia Geophysica et Geodaetica*, *22*(1), 50–62. https://doi.org/10.1007/BF01613632

Jelinek, V. (1981). Characterization of the magnetic fabric of rocks. *Tectonophysics*, *79*, 63–67.

Ji, W. B., Faure, M., Lin, W., Chen, Y., Chu, Y., & Xue, Z. H. (2017). Multiple emplacement and exhumation history of the Late Mesozoic Dayunshan–Mufushan batholith in southeast China and its tectonic significance: 1. Structural analysis and geochronological constraints. *Journal of Geophysical Research: Solid Earth*, *122*. https://doi.org/10.1002/2017JB014597

Ji, W. B., Lin, W., Faure, M., Chen, Y., Chu, Y., & Xue, Z. H. (2017). Origin of the Late Jurassic to Early Cretaceous peraluminous granitoids in the northeastern Hunan province (middle Yangtze region), south China: Geodynamic implications for the paleo-Pacific subduction. *Journal of Asian Earth Sciences*, *141*, 174–193. https://doi.org/10.1016/j.jseaes.2016.07.005

Ji, W. B., Lin, W., Faure, M., Shi, Y. H., & Wang, Q. C. (2017). The Early Cretaceous orogen-scale Dabieshan metamorphic core complex: Implications for extensional collapse of the Triassic HP–UHP orogenic belt in east-central China. *International Journal of Earth Sciences*, *106*(4), 1311–1340. https://doi.org/10.1007/s00531-016-1311-6

Jiang, Y. H., Wang, G. C., Liu, Z., Ni, C. Y., Qing, L., & Zhang, Q. (2015). Repeated slab advance-retreat of the Palaeo-Pacific Plate underneath SE China. *International Geology Review*, *57*(4), 472–491. https://doi.org/10.1080/00206814.2015.1017775

Jiang, Y. H., Zhao, P., Zhou, Q., Liao, S. Y., & Jin, G. D. (2011). Petrogenesis and tectonic implications of Early Cretaceous S- and A-type granites in the northwest of the Gan-Hang rift, SE China. *Lithos*, *121*(1–4), 55–73. https://doi.org/10.1016/j.lithos.2010.10.001

Joly, A., Faure, M., Martelet, G., & Chen, Y. (2009). Gravity inversion, AMS and geochronological investigations of syntectonic granitic plutons in the southern part of the Variscan French Massif Central. *Journal of Structural Geology*, *31*(4), 421–443. https://doi.org/10.1016/j.jsg.2009.01.004

Li, J. H., Zhang, Y. Q., Dong, S. W., & Johnston, S. T. (2014). Cretaceous tectonic evolution of south China: A preliminary synthesis. *Earth Science Reviews*, *134*, 98–136. https://doi.org/10.1016/j.earscirev.2014.03.008

Li, S. Z., Santosh, M., Zhao, G. C., Zhang, G. W., & Jin, C. (2012). Intracontinental deformation in a frontier of super-convergence: A perspective on the tectonic milieu of the South China Block. *Journal of Asian Earth Sciences*, *49*, 313–329. https://doi.org/10.1016/j.jseaes.2011.07.026

Li, X. H. (2000). Cretaceous magmatism and lithospheric extension in southeast China. *Journal of Asian Earth Sciences*, *18*(3), 293–305. https://doi.org/10.1016/S1367-9120(99)00060-7

Li, X. H., Li, W. X., Wang, X. C., Li, Q. L., Liu, Y., Tang, G. Q., … Wu, F. Y. (2010). SIMS U–Pb zircon geochronology of porphyry Cu–Au–(Mo) deposits in the Yangtze River Metallogenic Belt, eastern China: Magmatic response to early cretaceous lithospheric extension. *Lithos*, *119*(3–4), 427–438. https://doi.org/10.1016/j.lithos.2010.07.018

Li, X. H., Li, Z. X., Li, W. X., Liu, Y., Yuan, C., Wei, G. J., & Qi, C. S. (2007). U–Pb zircon, geochemical and Sr–Nd–Hf isotopic constraints on age and origin of Jurassic I- and A-type granites from central Guangdong, SE China: A major igneous event in response to foundering of a subducted flat-slab? *Lithos*, *96*(1–2), 186–204. https://doi.org/10.1016/j.lithos.2006.09.018

Li, Z., Qiu, J. S., & Yang, X. M. (2014). A review of the geochronology and geochemistry of late Yanshanian (cretaceous) plutons along the Fujian coastal area of southeastern China: Implications for magma evolution related to slab break-off and rollback in the cretaceous. *Earth Science Reviews*, *128*, 232–248. https://doi.org/10.1016/j.earscirev.2013.09.007

Li, Z. X., & Li, X. H. (2007). Formation of the 1300-km-wide intracontinental orogen and postorogenic magmatic province in Mesozoic south China: A flat-slab subduction model. *Geology*, *35*(2), 179–182. https://doi.org/10.1130/G23193A.1

Li, Z. X., Li, X. H., Wartho, J. A., Clark, C., Li, W. X., Zhang, C. L., & Bao, C. M. (2010). Magmatic and metamorphic events during the early Paleozoic Wuyi–Yunkai orogeny, southeastern south China: New age constraints and pressure-temperature conditions. *Geological Society of America Bulletin*, *122*(5–6), 772–793. https://doi.org/10.1130/B30021.1

Liang, W. T., Zhang, G. W., Bai, Y., Jin, C. S., & Nantasin, P. (2015). New insights into the emplacement mechanism of the Late Triassic granite plutons in the Qinling orogen: A structural study of the Mishuling pluton. *Geological Society of America Bulletin*, *127*(11–12), 1583–1603. https://doi.org/10.1130/B31187.1

Lin, W., Charles, N., Chen, K., Chen, Y., Faure, M., Wu, L., … Wang, Q. C. (2013). Late Mesozoic compressional to extensional tectonics in the Yiwulüshan massif, NE China and its bearing on the evolution of the Yinshan–Yanshan orogenic belt. Part II: Anisotropy of magnetic susceptibility and gravity modeling. *Gondwana Research*, *23*(1), 78–94. https://doi.org/10.1016/j.gr.2012.02.012

Lin, W., Faure, M., Chen, Y., Ji, W. B., Wang, F., Wu, L., … Wang, Q. C. (2013). Late Mesozoic compressional to extensional tectonics in the Yiwulüshan massif, NE China and its bearing on the evolution of the Yinshan–Yanshan orogenic belt. Part I: Structural analyses and geochronological constraints. *Gondwana Research*, *23*(1), 54–77. https://doi.org/10.1016/j.gr.2012.02.013

Lin, W., Ji, W. B., Faure, M., Wu, L., Li, Q. L., Shi, Y. H., … Wang, Q. C. (2015). Early cretaceous extensional reworking of the Triassic HP–UHP metamorphic orogen in eastern China. *Tectonophysics*, *662*, 256–270. https://doi.org/10.1016/j.tecto.2015.05.028

Lin, W., & Wang, Q. C. (2006). Late Mesozoic extensional tectonics in North China block: A crustal response to subcontinental mantle removal? *Bulletin de la Societe Geologique de France*, *177*(6), 287–297. https://doi.org/10.2113/gssgfbull.177.6.287

Lin, W., Wang, Q. C., & Chen, K. (2008). Phanerozoic tectonics of South China Block: New insights from the polyphase deformation in the Yunkai massif. *Tectonics*, *27*, TC6004. https://doi.org/10.1029/2007TC002207

Ling, M. X., Wang, F. Y., Ding, X., Hu, Y. H., Zhou, J. B., Zartman, R. E., … Sun, W. D. (2009). Cretaceous ridge subduction along the Lower Yangtze River belt, eastern China. *Economic Geology*, *104*(2), 303–321. https://doi.org/10.2113/gsecongeo.104.2.303

Liu, H. S., Chen, Y., Faure, M., Scaillet, B., Wang, B., Martelet, G., … Erdmann, S. (2016). Emplacement mechanism of the Middle-Late Jurassic Qitianling pluton and its implications on the Mesozoic tectonics of South China Block, EGU General Assembly Abstract.

Liu, J. L., Shen, L., Ji, M., Guan, H. M., Zhang, Z. C., & Zhao, Z. D. (2013). The Liaonan/Wanfu metamorphic core complexes in the Liaodong peninsula: Two stages of exhumation and constraints on the destruction of the North China Craton. *Tectonics*, *32*(5), 1121–1141. https://doi.org/10.1002/tect.20064

Liu, L., Xu, X. S., & Xia, Y. (2016). Asynchronizing paleo-Pacific slab rollback beneath SE China: Insights from the episodic Late Mesozoic volcanism. *Gondwana Research*, *37*, 397–407. https://doi.org/10.1016/j.gr.2015.09.009

Liu, Q., Yu, J. H., Wang, Q., Su, B., Zhou, M. F., Xu, H., & Cui, X. (2012). Ages and geochemistry of granites in the Pingtan–Dongshan Metamorphic Belt, coastal south China: New constraints on Late Mesozoic magmatic evolution. *Lithos*, *150*, 268–286. https://doi.org/10.1016/j.lithos.2012.06.031

Liu, S. F., Li, W. P., Wang, K., Qian, T., & Jiang, C. X. (2015). Late Mesozoic development of the southern Qinling–Dabieshan foreland fold-thrust belt, central China, and its role in continent–continent collision. *Tectonophysics*, *644–645*, 220–234.

Liu, X., Zhao, D. P., Li, S. Z., & Wei, W. (2017). Age of the subducting Pacific slab beneath East Asia and its geodynamic implications. *Earth and Planetary Science Letters*, *464*, 166–174. https://doi.org/10.1016/j.epsl.2017.02.024

Martelet, G., Debéglia, N., & Truffert, C. (2002). Homogénéisation et validation des corrections de terrain gravimétriques jusqu'à la distance de 167 km sur l'ensemble de la France (Updating and validating the French gravity terrain corrections out to a distance of 167 km). *Comptes Rendus Geoscience*, *334*(7), 449–454. https://doi.org/10.1016/S1631-0713(02)01779-0

Martín-Hernández, F., & Hirt, A. M. (2003). Paramagnetic anisotropy of magnetic susceptibility in biotite, muscovite and chlorite single crystals. *Tectonophysics*, *367*(1–2), 13–28. https://doi.org/10.1016/S0040-1951(03)00127-6

Müller, R. D., Seton, M., Zahirovic, S., Williams, S. E., Matthews, K. J., Wright, N. M., … Cannon, J. (2016). Ocean basin evolution and global-scale plate reorganization events since Pangea breakup. *Annual Review of Earth and Planetary Sciences*, *44*(1), 107–138. https://doi.org/10.1146/annurev-earth-060115-012211

Paterson, S. R., Fowler, T. K. Jr., Schmidt, K. L., Yoshinobu, A. S., Yuan, E. S., & Miller, R. B. (1998). Interpreting magmatic fabric patterns in plutons. *Lithos*, *44*(1–2), 53–82. https://doi.org/10.1016/S0024-4937(98)00022-X

Rochette, P., Jackson, M., & Aubourg, C. (1992). Rock magnetism and the interpretation of anisotropy of magnetic susceptibility. *Reviews of Geophysics*, *30*(3), 209–226. https://doi.org/10.1029/92RG00733

Seton, M., Müller, R. D., Zahirovic, S., Gaina, C., Torsvik, T., Shephard, G., … Chandler, M. (2012). Global continental and ocean basin reconstructions since 200 Ma. *Earth Science Reviews*, *113*(3–4), 212–270. https://doi.org/10.1016/j.earscirev.2012.03.002

Shu, L. S., Jahn, B. M., Charvet, J., Santosh, M., Wang, B., Xu, X. S., & Jiang, S. Y. (2014). Intraplate tectono-magmatism in the Cathaysia block (south China): Evidence from stratigraphic, structural, geochemical and geochronological investigations. *American Journal of Science*, *314*(1), 154–186. https://doi.org/10.2475/01.2014.05

Shu, L. S., Wang, B., Cawood, P. A., Santosh, M., & Xu, Z. Q. (2015). Early Paleozoic and Early Mesozoic intraplate tectonic and magmatic events in the Cathaysia block, south China. *Tectonics*, *34*(8), 1600–1621. https://doi.org/10.1002/2015TC003835

Shu, L. S., Zhou, X. M., Deng, P., Wang, B., Jiang, S. Y., Yu, J. H., & Zhao, X. X. (2009). Mesozoic tectonic evolution of the southeast China block: New insights from basin analysis. *Journal of Asian Earth Sciences*, *34*(3), 376–391. https://doi.org/10.1016/j.jseaes.2008.06.004

Talbot, J. Y., Faure, M., Chen, Y., & Martelet, G. (2005). Pull-apart emplacement of the Margeride granitic complex (French Massif Central). Implications for the late evolution of the Variscan orogen. *Journal of Structural Geology*, *27*(9), 1610–1629. https://doi.org/10.1016/j.jsg.2005.05.008

Tarling, D. H., & Hrouda, F. (1993). *The magnetic anisotropy of rocks*. London: Chapman & Hall.

Turrillot, P., Faure, M., Martelet, G., Chen, Y., & Augier, R. (2011). Pluton-dyke relationships in a Variscan granitic complex from AMS and gravity modelling. Inception of the extensional tectonics in the south Armorican domain (France). *Journal of Structural Geology*, *33*(11), 1681–1698. https://doi.org/10.1016/j.jsg.2011.08.004

Van der Voo, R., Van Hinsbergen, D. J. J., Domeier, M., Spakman, W., & Torsvik, T. H. (2015). Latest Jurassic–earliest Cretaceous closure of the Mongol–Okhotsk Ocean: A paleomagnetic and seismological–tomographic analysis. *Geological Society of America Special Papers*, *513*, 589–606.

Vigneresse, J. L. (1995). Control of granite emplacement by regional deformation. *Tectonophysics*, *249*(3–4), 173–186. https://doi.org/10.1016/0040-1951(95)00004-7

Wang, D. Z., & Shu, L. S. (2012). Late Mesozoic basin and range tectonics and related magmatism in southeast China. *Geoscience Frontiers*, *3*(2), 109–124. https://doi.org/10.1016/j.gsf.2011.11.007

Wang, F. Y., Ling, M. X., Ding, X., Hu, Y. H., Zhou, J. B., Yang, X. Y., … Sun, W. D. (2011). Mesozoic large magmatic events and mineralization in SE China: Oblique subduction of the Pacific Plate. *International Geology Review*, *53*(5–6), 704–726. https://doi.org/10.1080/00206814.2010.503736

Wang, L. X., Ma, C. Q., Zhang, C., Zhang, J. Y., & Marks, M. A. W. (2014). Genesis of leucogranite by prolonged fractional crystallization: A case study of the Mufushan complex, south China. *Lithos*, *206–207*, 147–163.

Wang, T., Guo, L., Zheng, Y. D., Donskaya, T., Gladkochub, D., Zeng, L. S., … Mazukabzov, A. (2012). Timing and processes of Late Mesozoic mid-lower-crustal extension in continental NE Asia and implications for the tectonic setting of the destruction of the North China Craton: Mainly constrained by zircon U–Pb ages from metamorphic core complexes. *Lithos*, *154*, 315–345. https://doi.org/10.1016/j.lithos.2012.07.020

Wang, T., Zheng, Y. D., Zhang, J. J., Zeng, L. S., Donskaya, T., Guo, L., & Li, J. B. (2011). Pattern and kinematic polarity of Late Mesozoic extension in continental NE Asia: Perspectives from metamorphic core complexes. *Tectonics*, *30*, TC6007. https://doi.org/10.1029/2011TC002896

Wang, Y. J., Fan, W. M., Zhang, G. W., & Zhang, Y. H. (2013). Phanerozoic tectonics of the South China Block: Key observations and controversies. *Gondwana Research*, *23*(4), 1273–1305. https://doi.org/10.1016/j.gr.2012.02.019

Wei, W., Chen, Y., Faure, M., Martelet, G., Lin, W., Wang, Q. C., … Hou, Q. L. (2016). An early extensional event of the South China Block during the Late Mesozoic recorded by the emplacement of the Late Jurassic syntectonic Hengshan composite granitic massif (Hunan, SE China). *Tectonophysics*, *672–673*, 50–67.

Wei, W., Chen, Y., Faure, M., Shi, Y. H., Martelet, G., Hou, Q. L., … Wang, Q. C. (2014). A multidisciplinary study on the emplacement mechanism of the Qingyang–Jiuhua massif in southeast China and its tectonic bearings. Part I: Structural geology, AMS and paleomagnetism. *Journal of Asian Earth Sciences*, *86*, 76–93. https://doi.org/10.1016/j.jseaes.2013.06.003

Wei, W., Martelet, G., Le Breton, N., Shi, Y. H., Faure, M., Chen, Y., … Wang, Q. C. (2014). A multidisciplinary study of the emplacement mechanism of the Qingyang–Jiuhua massif in southeast China and its tectonic bearings. Part II: Amphibole geobarometry and gravity modeling. *Journal of Asian Earth Sciences*, *86*, 94–105. https://doi.org/10.1016/j.jseaes.2013.09.021

Wong, J., Sun, M., Xing, G. F., Li, X. H., Zhao, G. C., Wong, K., … Wu, F. Y. (2009). Geochemical and zircon U–Pb and Hf isotopic study of the Baijuhuajian metaluminous A-type granite: Extension at 125–100 Ma and its tectonic significance for south China. *Lithos*, *112*(3–4), 289–305. https://doi.org/10.1016/j.lithos.2009.03.009

Wu, F. Y., Ji, W. Q., Sun, D. H., Yang, Y. H., & Li, X. H. (2012). Zircon U–Pb geochronology and Hf isotopic compositions of the Mesozoic granites in southern Anhui Province, China. *Lithos*, *150*, 6–25. https://doi.org/10.1016/j.lithos.2012.03.020

Yan, D. P., Zhou, M. F., Song, H. L., Wang, X. W., & Malpas, J. (2003). Origin and tectonic significance of a Mesozoic multi-layer over-thrust system within the Yangtze block (south China). *Tectonophysics*, *361*(3–4), 239–254. https://doi.org/10.1016/S0040-1951(02)00646-7

Yang, Y. T., Guo, Z. X., Song, C. C., Li, X. B., & He, S. (2015). A short-lived but significant Mongol–Okhotsk collisional orogeny in latest Jurassic–earliest cretaceous. *Gondwana Research*, *28*(3), 1096–1116. https://doi.org/10.1016/j.gr.2014.09.010

Zhang, D., Liu, W. C., Wu, G. G., Li, D. X., Di, Y. J., Zang, W. S., … Huang, H. J. (2008). Magnetic fabric and emplacement of the Fenghuangshan pluton, Tongling, Anhui Province, east-central China. *International Geology Review*, *50*, 1–14.

Zhou, X. M., & Li, W. X. (2000). Origin of Late Mesozoic igneous rocks in southeastern China: Implications for lithosphere subduction and underplating of mafic magmas. *Tectonophysics*, *326*(3–4), 269–287. https://doi.org/10.1016/S0040-1951(00)00120-7

Zhou, X. M., Sun, T., Shen, W. Z., Shu, L. S., & Niu, Y. L. (2006). Petrogenesis of Mesozoic granitoids and volcanic rocks in south China: A response to tectonic evolution. *Episodes*, *29*, 26–33.

Zhu, R. X., Xu, Y. G., Zhu, G., Zhang, H. F., Xia, Q. K., & Zheng, T. Y. (2012). Destruction of the North China Craton. *Science China Earth Sciences*, *55*(10), 1565–1587. https://doi.org/10.1007/s11430-012-4516-y